12-19-2023

A broadly reactive antibody targeting the N-terminal domain of SARS-CoV-2 spike confers Fc-mediated protection

Lucas J Adams
Washington University School of Medicine in St. Louis

Laura A VanBlargan
Washington University School of Medicine in St. Louis

Zhuoming Liu
Washington University School of Medicine in St. Louis

Pavlo Gilchuk
Vanderbilt University

Haiyan Zhao
Washington University School of Medicine in St. Louis

See next page for additional authors

Recommended Citation
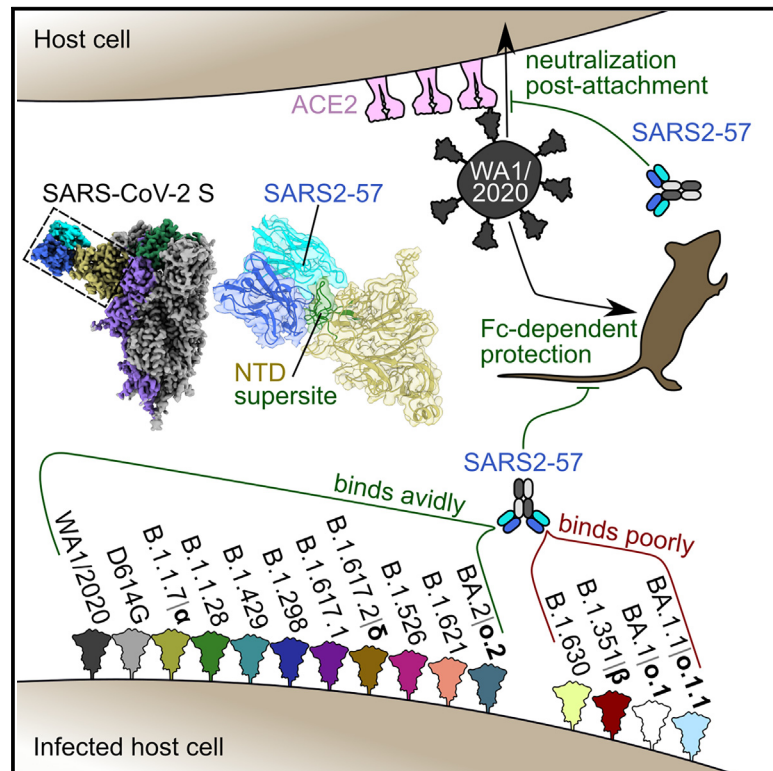
Authors

Lucas J Adams, Laura A VanBlargan, Zhuoming Liu, Pavlo Gilchuk, Haiyan Zhao, Rita E Chen, Saravanan Raju, Zhenlu Chong, Bradley M Whitener, Swathi Shrihari, Prashant N Jethva, Michael L Gross, James E Crowe Jr., Sean P J Whelan, Michael S Diamond, and Daved H Fremont

Article

A broadly reactive antibody targeting the N-terminal domain of SARS-CoV-2 spike confers Fc-mediated protection

Graphical abstract

Authors
Lucas J. Adams, Laura A. VanBlargan, Zhuoming Liu, ..., Sean P.J. Whelan, Michael S. Diamond, Daved H. Fremont

Correspondence
mdiamond@wustl.edu (M.S.D.), fremont@wustl.edu (D.H.F.)

In brief

Adams et al. describe a neutralizing mAb, SARS2-57, that efficiently binds cells infected by many SARS-CoV-2 variants and confers Fc-mediated protection in mice. Structural analysis demonstrates that SARS2-57 targets the NTD, revealing the basis for variant recognition and immune evasion.

Highlights

- NTD mAbs block SARS-CoV-2 infection at a post-attachment step

- SARS2-57 mAb recognizes most variants and confers Fc-mediated protection in mice

- Cryo-EM reveals SARS2-57 binds loops N3 and N5 of the NTD supersite

- Cryo-EM reveals the basis of SARS2-57 variant recognition and immune evasion

CellPress

Article

A broadly reactive antibody targeting the N-terminal domain of SARS-CoV-2 spike confers Fc-mediated protection

Lucas J. Adams,[1,8] Laura A. VanBlargan,[2,8] Zhuoming Liu,[3,8] Pavlo Gilchuk,[4] Haiyan Zhao,[1] Rita E. Chen,[1,2] Saravanan Raju,[1] Zhenlu Chong,[2] Bradley M. Whitener,[2] Swathi Shrihari,[2] Prashant N. Jethva,[5] Michael L. Gross,[5] James E. Crowe, Jr.,[4] Sean P.J. Whelan,[3] Michael S. Diamond,[1,2,3,7,*] and Daved H. Fremont[1,3,6,7,9,*]

[1]Department of Pathology and Immunology, Washington University School of Medicine, St. Louis, MO 63110, USA
[2]Department of Medicine, Washington University School of Medicine, St. Louis, MO, USA
[3]Department of Molecular Microbiology, School of Medicine, Washington University in St. Louis, St. Louis, MO, USA
[4]Vanderbilt Vaccine Center, Vanderbilt University Medical Center, Nashville, TN 37232, USA
[5]Department of Chemistry, Washington University, St. Louis, MO 63130, USA
[6]Department of Biochemistry and Molecular Biophysics, Washington University School of Medicine, St. Louis, MO 63110, USA
[7]Andrew M. and Jane M. Bursky Center for Human Immunology and Immunotherapy Programs, Washington University School of Medicine, St. Louis, MO, USA
[8]These authors contributed equally
[9]Lead contact
*Correspondence: mdiamond@wustl.edu (M.S.D.), fremont@wustl.edu (D.H.F.)
https://doi.org/10.1016/j.xcrm.2023.101305

SUMMARY

Most neutralizing anti-SARS-CoV-2 monoclonal antibodies (mAbs) target the receptor binding domain (RBD) of the spike (S) protein. Here, we characterize a panel of mAbs targeting the N-terminal domain (NTD) or other non-RBD epitopes of S. A subset of NTD mAbs inhibits SARS-CoV-2 entry at a post-attachment step and avidly binds the surface of infected cells. One neutralizing NTD mAb, SARS2-57, protects K18-hACE2 mice against SARS-CoV-2 infection in an Fc-dependent manner. Structural analysis demonstrates that SARS2-57 engages an antigenic supersite that is remodeled by deletions common to emerging variants. In neutralization escape studies with SARS2-57, this NTD site accumulates mutations, including a similar deletion, but the addition of an anti-RBD mAb prevents such escape. Thus, our study highlights a common strategy of immune evasion by SARS-CoV-2 variants and how targeting spatially distinct epitopes, including those in the NTD, may limit such escape.

INTRODUCTION

Severe acute respiratory syndrome coronavirus 2 (SARS-CoV-2), the causative agent of coronavirus disease 2019 (COVID-19), emerged in late 2019 in Wuhan, China, but has since spread worldwide, causing over 768 million infections and 6.9 million deaths (https://covid19.who.int/). The COVID-19 pandemic spurred an unprecedented global effort to develop preventive or therapeutic countermeasures, which resulted in the rapid deployment of vaccines and therapeutic monoclonal antibodies (mAbs).[1–8] However, SARS-CoV-2 variants emerged with resistance to all antibodies used clinically, highlighting the need for continued antibody discovery and development.[2,9–12]

Anti-SARS-CoV-2 mAbs have been characterized extensively in neutralization and animal studies as part of pre-clinical development efforts. Most studies have focused on antibodies targeting the receptor binding domain (RBD) of the SARS-CoV-2 spike (S) protein, typically preventing binding of S with its receptor angiotensin-converting enzyme 2 (ACE2),[13–35] although neutralizing anti-RBD mAbs that do not compete with ACE2 also have been

described.[36] Indeed, all anti-SARS-CoV-2 mAbs that were used clinically target the RBD.[2,3,8] Some neutralizing mAbs targeting the N-terminal domain (NTD) or S2 domain of spike have been identified[17,25,37–42]; however, their precise mechanism of neutralization remains less clear but might involve inhibition of S2′ cleavage or disruption of the S trimer.[43,44] SARS-CoV-2 can escape from both RBD-directed and NTD-directed antibodies,[25,42,45–48] and many emerging SARS-CoV-2 variants harboring mutations or deletions in these regions demonstrate resistance to individual mAbs as well as polyclonal serum from convalescent or vaccinated individuals.[9,49–53] Thus, it is critical to define further how mAbs targeting neutralizing epitopes inhibit infection, how SARS-CoV-2 evades humoral immunity, and how antibody-based therapies can be designed to minimize or prevent this escape.

Here, we describe a panel of mAbs targeting the NTD or other non-RBD epitopes of SARS-CoV-2 S. We evaluated their mechanism of inhibition and showed that neutralizing mAbs targeting the NTD inhibit viral entry at a post-attachment step. A subset of anti-NTD mAbs binds avidly to the surface of infected cells for possible Fc-dependent engagement by immune cells. One mAb in this

Group	Ab:	Isotype	ELISA reactivity			Neutralization		Cross-reactivity		% ACE2 inhibition	% reference mAb binding inhibition	
			Spike	NTD	RBD	Percent inhibition	EC50 ng/ml	SARS2 (OD450)	SARS1 (OD450)		CR3022	COV2-2676
1	SARS2-57	IgG1	4	3.4	0.129	52	3510	1.6	0.1	4	14	98
	SARS2-35	IgG1	4	3.4	0.271	44	8831	1.5	0.0	1	10	95
	SARS2-50	IgG1	4	3.3	0.151	40	>LoD	1.8	0.0	5	10	93
	SARS2-56	IgG1	4	2.7	0.146	35	>LoD	1.6	0.0	1	9	89
	SARS2-47	IgG1	4	2.9	0.169	32	>LoD	1.6	0.0	5	9	82
	SARS2-40	IgG1	4	2.1	0.13	36	11790	1.6	0.0	1	-1	71
2	SARS2-29	IgG1	4	1.6	0.087	57	609	1.4	0.0	4	9	-11
	SARS2-69	IgG1	4	1.1	0.156	41	3595	1.5	0.0	5	5	19
	SARS2-11	IgG1	4	2.0	0.51	57	913	1.2	0.0	5	10	-7
	SARS2-12	IgG1	4	3.2	0.737	42	2229	1.5	0.1	4	6	-11
	SARS2-30	IgG1	4	2.4	0.223	26	1997	1.5	0.0	3	12	-10
	SARS2-68	IgG1	4	1.6	0.181	2	1811	1.5	0.1	5	15	-13
3	SARS2-36	IgG1	4	0.1	0.558	66	2438	1.4	0.1	9	82	8
	SARS2-24	IgG1	4	0.1	0.584	58	2622	0.8	0.2	4	3	13
	SARS2-51	IgG1	4	0.8	0.159	34	2200	1.7	0.0	3	-1	19
	SARS2-28	IgG1	4	0.1	0.218	19	>LoD	1.4	1.5	4	1	9
	SARS2-13	IgG1	4	0.1	0.189	28	>LoD	1.6	1.7	6	7	6
	SARS2-20	IgG2b	4	0.1	0.219	34	>LoD	1.3	1.2	3	5	4
	SARS2-17	IgG1	4	0.1	0.192	-7	>LoD	1.8	1.8	7	3	9
	SARS2-26	IgG1	4	0.1	0.142	16	>LoD	1.6	1.6	5	6	9
	SARS2-64	IgG1	4	0.1	0.195	-2	>LoD	1.7	1.8	3	17	23
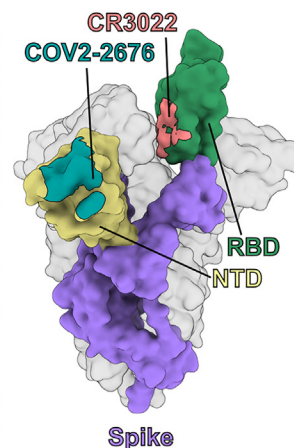
Figure 1. Panel of anti-SARS-CoV-2 mAbs

Hybridoma supernatants from the panel of anti-SARS-CoV-2 murine mAbs were assayed for inhibition of SARS-CoV-2 by focus-reduction neutralization test (FRNT), cross-reactivity to SARS-CoV-1 S protein, and ability to inhibit SARS-CoV-2 S protein binding to hACE2 or a panel of reference human mAbs through competition ELISA. MAbs are grouped by reference mAb competition properties. EC$_{50}$ values reflect neutralization experiments performed with purified mAbs. Data represent the mean (or geometric mean for EC$_{50}$ values) from two to four experiments. Beside the table, an approximate epitope is illustrated for each reference mAb, with that of CR3022 (PDB 7LOP) in pink and COV2-2676 (EMDB: EMD-23155) in blue.

class, SARS2-57, protected human ACE2 (hACE2)-transgenic mice against an ancestral SARS-CoV-2 strain (WA1/2020) as prophylaxis or post-exposure therapy in an Fc-dependent fashion. Cryo-electron microscopy (cryo-EM) analysis of SARS2-57 Fab bound to SARS-CoV-2 S protein established binding to loops N3 and N5, consistent with a previously described antigenic supersite on the NTD.[37,54] Using a chimeric vesicular stomatitis virus (VSV) displaying the S protein of SARS-CoV-2 (VSV-eGFP-SARS-CoV-2-S), we generated escape mutations to SARS2-57 within these same loops. However, the addition of an anti-RBD mAb prevented this escape. SARS2-57 retained binding to the S proteins of most emerging SARS-CoV-2 variants, including B.1.1.7 (Alpha), B.1.1.28 (Gamma), B.1.617.1 (Kappa), B.1.617.2 (Delta), B.1.526 (Iota), B.1.429 (Epsilon), B.1.621 (Mu), B.1.1.298, and BA.2 (Omicron subvariant) but not B.1.351 (Beta), B.1.630, BA.1 (Omicron), or BA1.1. Our analysis also provides a structural basis for the failure of SARS-57 to recognize B.1.351, B.1.630, and BA.1/BA.1.1 S proteins, which harbor deletions that likely deform the supersite targeted by SARS2-57 and other neutralizing NTD-directed antibodies.

RESULTS

### Development and characterization of anti-SARS-CoV-2 mAbs

We previously generated a panel of anti-SARS-CoV-2 mAbs from BALB/c mice immunized and boosted with the recombinant RBD and/or ectodomain of the S protein. Of the 64 anti-SARS-CoV-2 mAbs obtained, 43 of these bound to RBD and have been described.[32] Of the 21 mAbs that did not recognize purified RBD, 12 bound to the NTD and nine did not, likely recognizing epitopes on S outside of these two domains or that are inacces-

sible on the recombinant proteins (Figure 1). The murine mAbs were evaluated by competition-binding analysis to S protein using a previously characterized neutralizing human mAb against the NTD, COV2-2676[42] or a mAb that binds the base of the RBD, CR3022[55] (Figure 1). Of the 12 NTD-binding mAbs in our panel, six competed with COV2-2676, whereas the six others did not compete with either COV2-2676 or CR3022. Of the non-RBD, non-NTD-binding mAbs, only one competed with one of the tested mAbs: SARS2-36, which competes with CR3022, and thus likely binds an epitope that overlaps with CR3022 despite not binding to recombinant RBD protein. Based on the domain binding and competition analyses, we classified mAbs into three competition groups (Figure 1).

One potential mechanism of antibody-mediated neutralization of SARS-CoV-2 is through inhibition of viral S protein binding to the ACE2 receptor. We characterized the 21 mAbs in our non-RBD-binding panel for their ability to inhibit binding of S protein to purified ACE2 *in vitro* (Figure 1). None of these mAbs blocked the S-ACE2 interaction, likely because their epitopes are distant from the ACE2 receptor binding motif.

Neutralizing activity of anti-SARS-CoV-2 mAbs

We measured the neutralizing potency of the panel of anti-SARS-CoV-2 mAbs by a focus-reduction neutralization test (FRNT) with serial dilutions of hybridoma cell supernatants. The antibody levels in hybridoma supernatant were quantified by ELISA and used to calculate the concentrations that inhibited SARS-CoV-2 WA1/2020 infection. Several of the mAbs in the NTD-binding groups (both COV2-2676-competing and -non-competing groups) and the non-RBD/non-NTD competing groups were weakly neutralizing (half-maximal inhibition; EC$_{50}$ > 500 ng/mL) (Figure 1). A subset of mAbs from each group
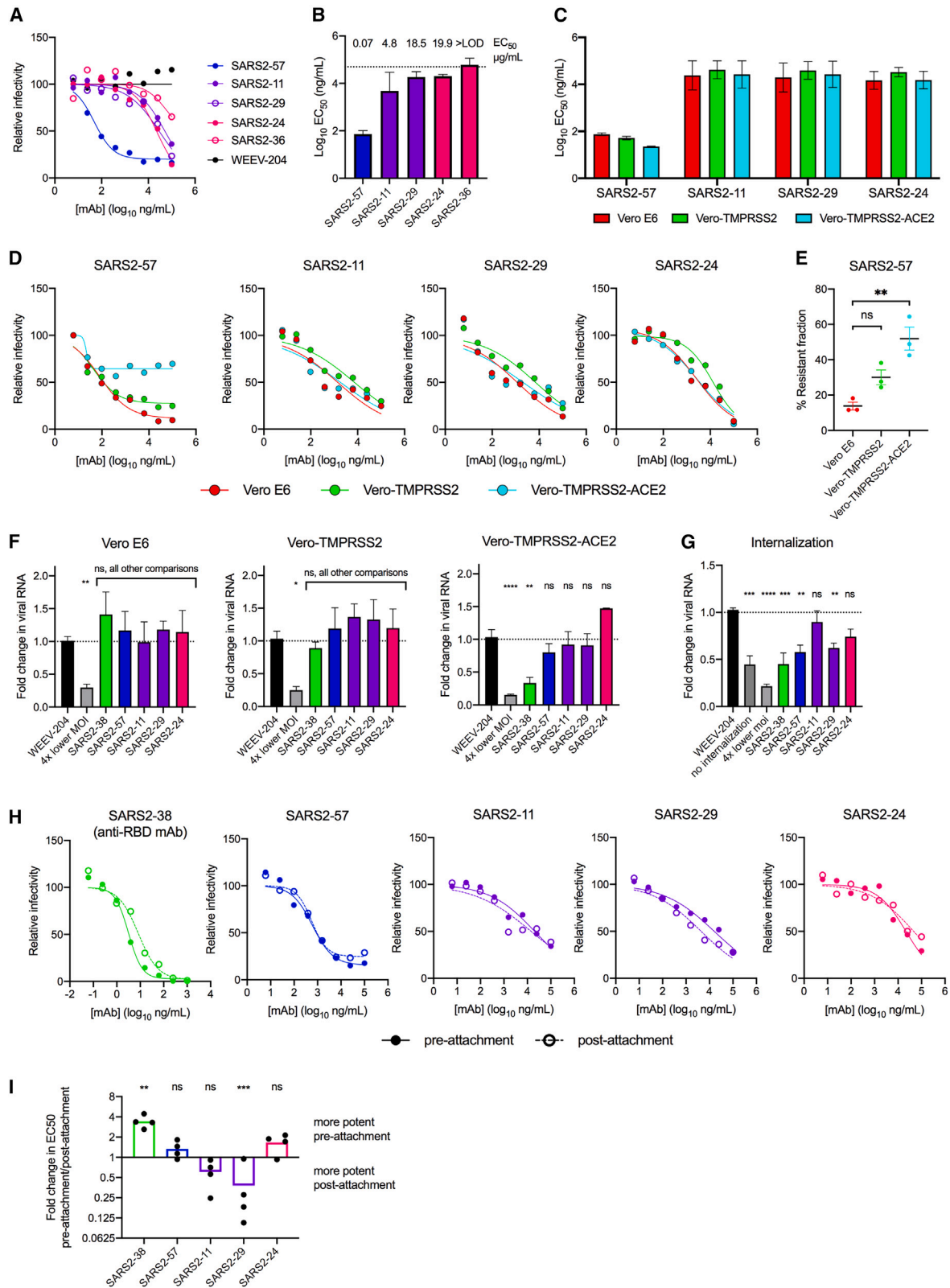
(including SARS2-11, SARS2-24, SARS2-29, SARS2-36, and SARS2-57) was selected for more detailed study based on the neutralization potency of antibodies in the hybridoma supernatant. The five mAbs were purified and retested for neutralization using a full dose-response analysis in Vero E6 cells (Figures 2A and 2B). SARS2-57 was the most potently neutralizing (EC$_{50}$: 73 ng/mL), although a resistant fraction of ~18% was present at saturating antibody concentrations (Figures 2A and 2B). The remaining NTD-binding and non-NTD/non-RBD-binding mAbs tested displayed less inhibitory potency (>5 μg/mL EC$_{50}$ values), with SARS2-36 showing no detectable neutralization at the highest concentration tested (100 μg/mL).

Cell type-dependent neutralization by an NTD-binding anti-SARS-CoV-2 mAb

Because SARS2-57 exhibited a neutralization-resistant fraction in Vero E6 cells, we expanded our functional analysis by assessing its activity in two additional cell types: Vero cells expressing TMPRSS2 (Vero-TMPRSS2) or Vero cells expressing TMPRSS2 and hACE2 (Vero-TMPRSS2-ACE2). The other neutralizing mAbs in the panel (SARS2-11, SARS2-24, and SARS2-29) were also included in this analysis. Whereas the EC$_{50}$ values across the different cellular substrates did not vary for SARS2-57 (Figures 2C and 2D), the neutralization-resistant fraction increased from 14% on Vero E6 cells to 30% (p = 0.08) on Vero-TMPRSS2 cells and 52% (p < 0.01) on Vero-TMPRSS2-hACE2 cells (Figures 2D and 2E). This finding was not seen with SARS2-11, SARS2-24, or SARS2-29, which maintained similar levels of neutralization across cellular substrates (Figure 2D). These data indicate that the expression levels of viral entry factors influence the neutralization-resistant fraction observed for SARS2-57.

Mechanism of neutralization by anti-SARS-CoV-2 mAbs

We tested the ability of the mAbs to block virus attachment to Vero, Vero-TMPRSS2, or Vero-TMPRSS2-hACE2 cells. An anti-RBD, hACE2-blocking mAb, SARS2-38,[32] was included as a control for these experiments. Notably, none of the NTD mAbs or non-NTD/non-RBD mAbs blocked virus attachment to Vero, Vero-TMPRSS2, or Vero-TMPRSS2-ACE2 cells (Figure 2F). In comparison, the RBD-binding mAb SARS2-38 blocked virus attachment to Vero-TMPRSS2-ACE2 cells. (Figure 2F, right). We next tested the ability of the mAbs to block viral entry at a later step using a virus internalization assay.[32] Both the RBD mAb SARS2-38 and NTD mAbs SARS2-29 and SARS2-57 reduced levels of virus internalized in Vero E6 cells (Figure 2G).

These data suggest that the anti-NTD mAbs can inhibit infection at a post-attachment step in the viral entry pathway.

To gain further support for this hypothesis, we compared the neutralization potency of the mAbs when added before or after virus absorption to Vero E6 cell monolayer cultures. All mAbs retained neutralizing activity when added post-attachment, although the potency of anti-RBD mAb SARS2-38 was reduced by ~4-fold relative to pre-attachment neutralization titers (Figures 2H and 2I). The anti-NTD mAbs SARS2-11 and SARS2-57, and the non-RBD/non-NTD mAb SARS2-24, neutralized SARS-CoV-2 with similar potencies when administered pre- or post-attachment (Figures 2H and 2I). Thus, mAbs that do not block S protein-ACE2 interaction or attachment can neutralize SARS-CoV-2 infection when added at a post-attachment step. This result is consistent with the behavior of previously described human NTD mAbs.[42] Unexpectedly, the NTD mAb SARS2-29 showed a slight 2.6-fold increase (p < 0.001) in neutralization potency when added post-attachment, which may indicate that its epitope is exposed more efficiently following virus interaction with the cell surface.

To further evaluate the mechanism of post-attachment neutralization by anti-NTD mAbs, we assessed the ability of mAb SARS2-57 to block S protein-mediated syncytia formation, as has been described for other NTD-specific mAbs.[54] We infected Vero E6-TMPRSS2 cells with VSV-SARS-CoV-2 chimeric virus encoding wild-type (WT) (D614G) or Omicron (BA.1) S protein and used fluorescence imaging to monitor cell-cell fusion in the presence or absence of SARS2-57 (Figure S1). Consistent with previous findings, VSV-SARS-CoV-2 BA.1 did not induce robust syncytia formation.[56] In contrast, cells infected with VSV-SARS-CoV-2 D614G formed syncytia, an effect impaired by SARS2-57 treatment. These findings suggest that some anti-NTD mAbs may neutralize infection post-attachment by preventing viral fusion or cell-to-cell spread.

Anti-SARS-CoV-2 mAbs bind to the surface of SARS-CoV-2-infected cells

In additional to virion neutralization, antibodies can confer protection through Fc-effector function mechanisms.[28,42,57–61] Antibodies that bind to S proteins on the surface of cells can trigger antibody-dependent cell-mediated cytotoxicity and cellular phagocytosis as well as clearance of infected cells. Accordingly, we investigated the ability of anti-RBD, anti-NTD, and non-RBD/non-NTD-binding mAbs to bind to the surface of SARS-CoV-2-infected Vero E6 cells using flow cytometry. The anti-RBD mAbs all stained infected cells relatively equivalently

---

Figure 2. Neutralization by anti-SARS-CoV-2 mAbs

(A–E) Anti-SARS-CoV-2 mAbs were assayed for neutralization by FRNT against SARS-CoV-2 using Vero E6 cells (A and B) or comparing Vero E6 cells with Vero-TMPRSS2 and Vero-hACE2-TMPRSS2 cells (C–E). (A and D) Representative dose-response curves are shown; error bars represent the range from two technical replicates. Data are from three to four experiments. (B and C) Geometric mean EC$_{50}$ values are shown.

(E) Neutralization-resistant fraction of SARS2-57 dose-response curves.

(F) Anti-SARS-CoV-2 mAbs were assayed for attachment inhibition of SARS-CoV-2 to Vero E6, Vero-TMPRSS2, or Vero-hACE2-TMPRSS2 cells. Data are from three experiments.

(G) Anti-SARS-CoV-2 mAbs were assayed for inhibition of virus internalization in Vero E6 cells. Data are from four experiments.

(H and I) Anti-SARS-CoV-2 mAbs were assayed for pre- or post-attachment neutralization of SARS-CoV-2 using Vero E6 cells. An anti-RBD mAb, SARS2-38, is included as a control. (H) Representative dose-response curves are shown. Error bars represent the range from two technical replicates. (I) Fold change in EC$_{50}$ values for pre-attachment over post-attachment neutralization. Error bars represent standard error of the mean (SEM) from four experiments. (I) ANOVA with Sidak's post-test comparing pre- versus post-attachment EC$_{50}$ values for each mAb; (F) and (G) one-way ANOVA with Dunnett's post-test compared mAb treatment with isotype control mAb treatment. ns, not significant; *p < 0.05; **p < 0.01; ***p < 0.001, ****p < 0.0001.

A

B

C

D
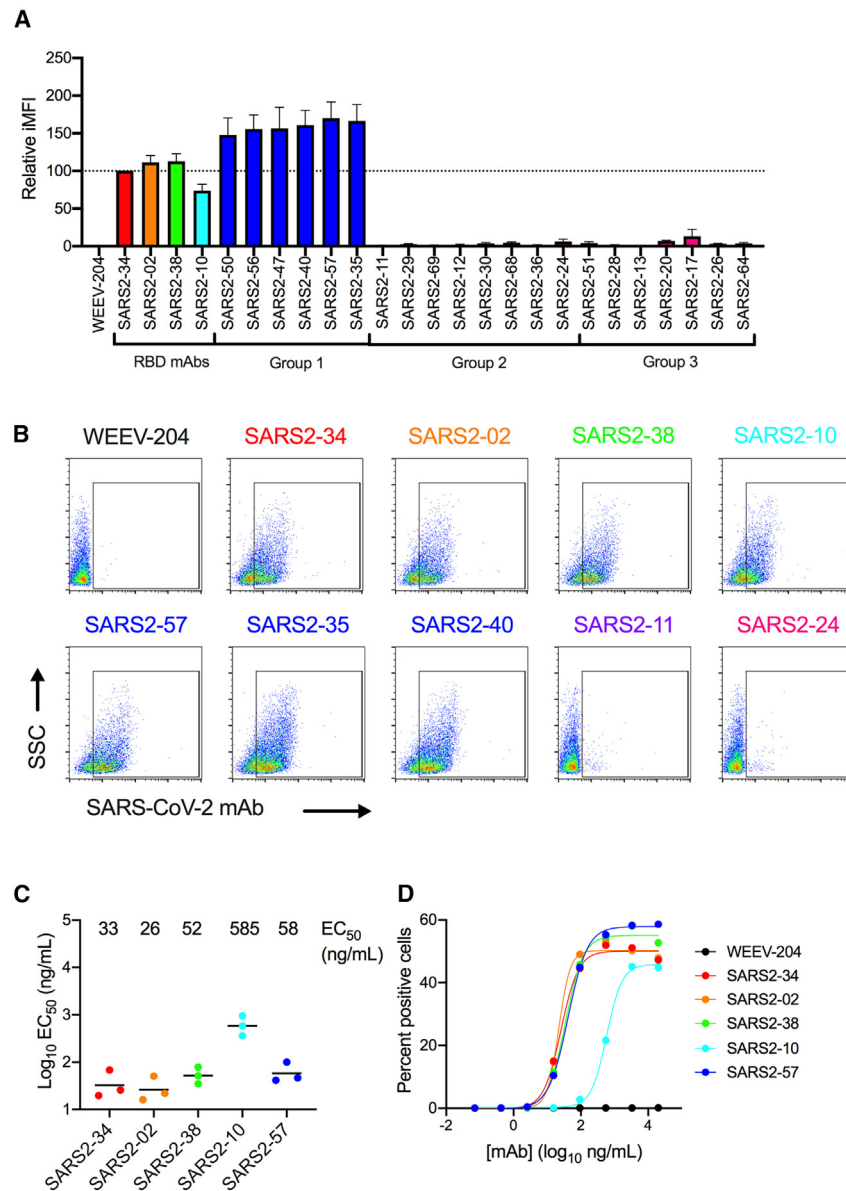
Figure 3. Staining of S protein on the surface of infected cells by anti-SARS-CoV-2 mAbs

(A and B) Vero cells infected with SARS2-CoV-2 were stained with the indicated anti-SARS-CoV-2 mAbs (10 μg/mL) and analyzed by flow cytometry. Positively stained cells were gated, and their integrated mean fluorescence intensity (iMFI) was determined (MFI × percent positive cells). (A) The mean relative iMFI from three experiments. Relative iMFI for each experiment was determined by normalizing iMFI values to a representative anti-RBD mAb, SARS2-34. (B) Representative flow cytometry plots with positive gates are shown.

(C and D) SARS-CoV-2-infected cells were stained with serial dilutions of anti-SARS-CoV-2 mAbs, and the EC_{50} values for the percent of positively stained cells were determined. (C) Mean EC_{50} values for each mAb. Error bars represent SEM from three experiments. (D) Representative dose-response curves are shown.

34, SARS2-02, SARS2-38, and SARS2-10.[32] Anti-RBD mAbs SARS2-34, SARS2-38, and SARS2-02 had EC_{50} values for cell surface staining in the range of 26–52 ng/mL, which was similar to the 58 ng/mL value measured with the anti-NTD mAb SARS2-57 (Figures 3C and 3D). Anti-RBD mAbs SARS2-10 showed ~10-fold less potent binding (EC_{50} value of 585 ng/mL) to the cell surface. These data indicate that NTD and RBD epitopes are exposed on cell surface-associated S proteins for possible recognition by antibodies and immune cells.

## mAbs protect against SARS-CoV-2 challenge *in vivo*

We next tested the anti-SARS-CoV-2 mAbs for protection against virus challenge *in vivo*. Eight- to 10-week-old K18-human hACE2 transgenic mice were administered a single 100-μg dose (~5 mg/kg) of anti-SARS-CoV-2 mAb as prophylaxis 24 h prior to intra-nasal inoculation with 10^3 ffu of SARS-CoV-2 strain WA1/2020. Mice treated with the isotype control mAb (murine mAb WEEV-204) began losing weight at 4 days post-infection (dpi) and continued to lose up to 25% body weight for the duration of the study, which was terminated at 7 dpi (Figure 4A). Group 1 anti-NTD mAb SARS2-57 protected mice from weight loss following SARS-CoV-2 infection (Figure 4A), whereas the group 2 anti-NTD mAbs SARS2-11 and SARS2-29 and group 3 non-NTD/non-RBD mAb SARS-36 did not protect against weight loss (Figure 4A).

We measured the effect of mAb treatment on viral burden by qRT-PCR in the nasal washes and lungs on 7 dpi. Mice treated with SARS2-57 had an ~50-fold reduction in viral load in the nasal wash and 20-fold reduction in the lung relative to isotype control mAb-treated mice (Figures 4B and 4C). SARS2-29, SARS2-11,

(Figures 3A and 3B). In comparison, staining of infected cells with some of the group 1 NTD-binding mAbs (including SARS2-57) was 60%–80% higher than the anti-RBD mAbs (Figures 3A and 3B). However, we did not detect binding of any group 2 anti-NTD mAbs (including SARS2-11 and SARS2-29) to the surface of infected cells (Figures 3A and 3B). Thus, some anti-NTD antibodies bind to SARS-CoV-2 infected cells better than the more potently neutralizing RBD mAbs; however, the epitopes of anti-NTD mAbs that do not compete with COV2-2676 are absent or obscured on the surface of infected cells. Group 3 non-RBD/non-NTD-binding mAbs likewise failed to bind to the surface infected cells (Figures 3A and 3B).

To further characterize the binding properties of the mAbs to S protein on the cell surface, we performed a dose-response analysis of anti-NTD mAb SARS2-57 and anti-RBD mAbs SARS2-
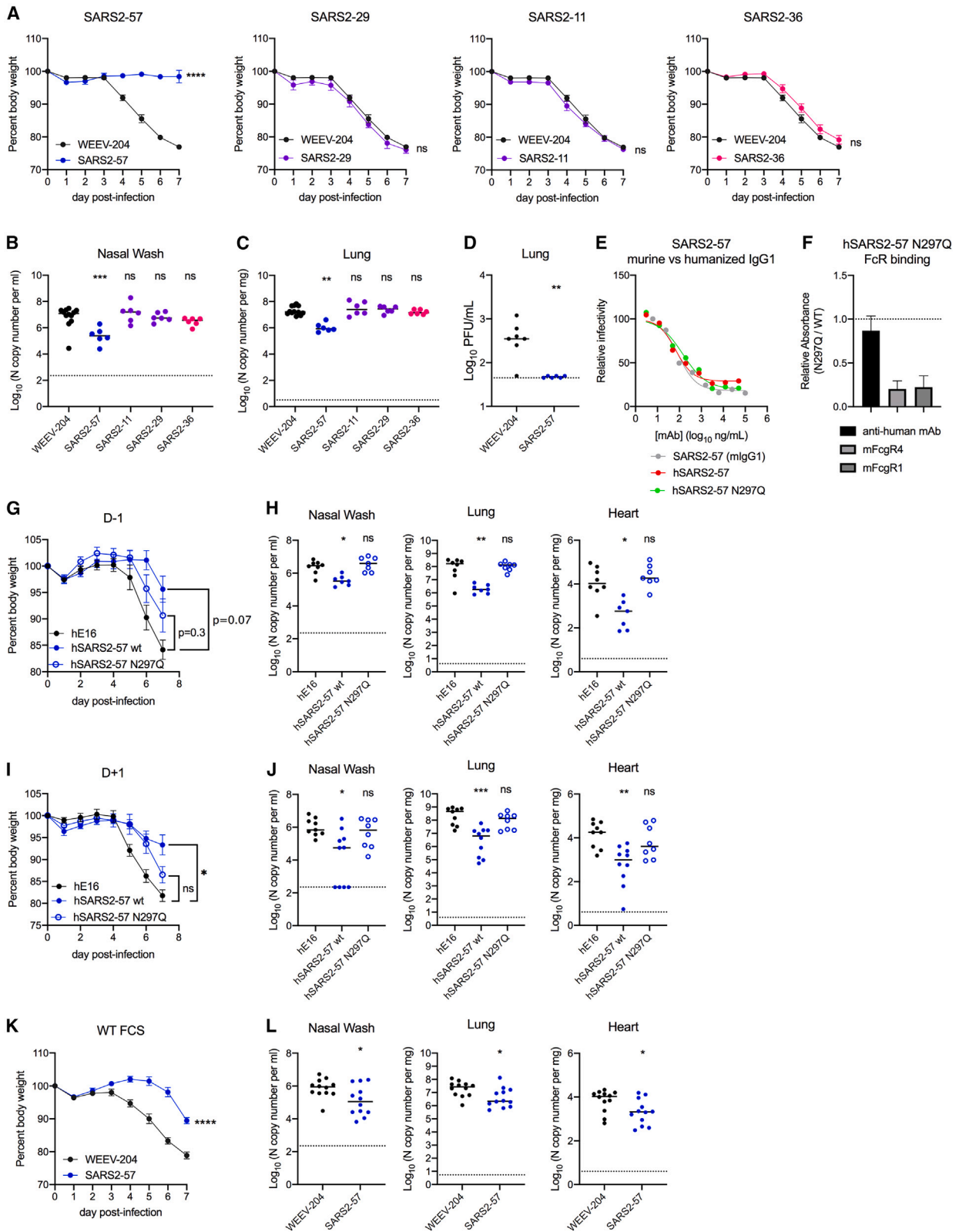
(legend on next page)

and SARS2-36 treatments had no effect on viral load in either the nasal wash or lung (Figures 4B and 4C). We also measured effects of SARS2-57 mAb treatment on the infectious viral load in the lung by plaque assay. SARS2-57 reduced the amount of infectious virus in the lung to the limit of detection of the assay (Figure 4D).

In the K18-hACE2 mouse model, cytokine and chemokine levels are markers of inflammatory and pathological outcomes.[62] For a subset of representative mAbs (SARS2-11, SARS2-57, and isotype control), we measured the levels of cytokines and chemokines in lung tissue homogenates at 7 dpi relative to naive mice. SARS2-11-treated mice showed similar induction of cytokines and chemokines relative to control mAb-treated mice (Figures S2A and S2B). SARS2-57-treated mice also showed upregulation, but the levels were significantly lower than isotype control mAb-treated mice for many of the cytokines and chemokines tested, including interferon (IFN)γ, tumor necrosis factor (TNF)-α, and interleukin (IL)-6 (Figure S2B).

Next, we tested the role of Fc-effector functions in the prophylactic and therapeutic efficacy of SARS2-57. SARS2-57 is a murine immunoglobulin (Ig)G1, an isotype that binds relatively poorly to murine Fcγ receptors and lacks strong Fc-effector function.[63] Because Fc-effector functions can contribute to the therapeutic activity of anti-SARS2-CoV-2 neutralizing mAbs,[28,42,57–59] we cloned the variable region of SARS2-57 into a human IgG1 backbone (referred to as hSARS2-57) and verified the neutralizing activity of this chimeric mouse-human antibody (Figure 4E). We also engineered hSARS2-57 with an N297Q mutation that disrupts Fcγ receptor and complement interactions.[64] We confirmed these properties by testing binding of hSARS2-57 and hSARS2-57 N297Q to murine FcγRI and FcγRIV by ELISA (Figure 4F).

We first tested the prophylactic efficacy of hSARS2-57 and hSARS2-57 N297Q by treating K18-hACE2 mice with a 100-μg ($\sim$5 mg/kg) dose of either mAb or an isotype control mAb and then inoculating them 24 h later with 10^3 ffu of SARS-CoV-2 by an intranasal route. Mice treated with hSARS2-57 lost less body weight than mice treated with hSARS2-57 N297Q (Figure 4G). Additionally, treatment with hSARS2-57 reduced viral loads in the nasal wash, lung, and heart, whereas hSARS2-57 N297Q treatment did not diminish viral loads compared with isotype control-treated animals (Figure 4H). To test the therapeutic efficacy of hSARS2-57, we inoculated K18-hACE2 mice with 10^3 ffu of SARS-CoV-2 strain WA1/2020, and 24 h later administered a single 200-μg ($\sim$10 mg/kg) dose of hSARS2-57, hSARS2-57 N297Q, or isotype control mAb. Whereas mice treated with the isotype control mAb lost around 20% of their initial body weight over this time frame, mice treated with hSARS2-57 lost on average only $\sim$7% of their initial body weight; mice treated with hSARS2-57 N297Q showed less protection against weight loss, losing $\sim$13% of their initial body weight (Figure 4I). Moreover, mice treated with hSARS2-57 had a 70-fold reduction in viral load in the lung at 7 dpi relative to isotype control mAb-treated mice ($p < 0.001$), an 18-fold reduction in the heart ($p < 0.01$) and a 12-fold reduction in the nasal wash ($p < 0.05$) (Figure 4J). In contrast, mice treated with hSARS2-57 N297Q showed no significant reduction in viral titers relative to control mAb-treated mice, confirming a role for Fc-effector functions in mediating the therapeutic efficacy of anti-SARS-CoV-2 mAbs. Together, these data indicate that SARS2-57 confers protection against SARS2-CoV-2 challenge as both prophylaxis and therapy in an Fc-dependent manner.

Deep sequencing analysis revealed that the *in vivo* studies described above were completed using a stock of WA1/2020 with a mutated furin cleavage site (FCS). While mutation of the FCS does not affect neutralization by NTD or RBD mAbs, it can impact the virulence of SARS-CoV-2 *in vivo* (Johnson et al.[65]). As such, we repeated prophylaxis studies with a WA1/2020 stock with a sequence-confirmed, intact FCS sequence. Mice treated with SARS2-57 maintained body weight until 7 dpi, at which point they lost $\sim$10% body weight, significantly less than observed for isotype-treated mice (Figure 4K). Mice treated with SARS2-57 also had reduced viral RNA levels in the nasal wash, lung, and heart at 7 dpi (Figure 4L). Thus, SARS2-57 protects mice against SARS-CoV-2 strains with intact or mutated FCS.

Figure 4. MAbs protect against SARS-CoV-2 infection *in vivo*

(A–D) K18-hACE2 transgenic mice were passively administered 100 μg ($\sim$5 mg/kg) of the indicated mAb by intraperitoneal injection 24 h prior to intranasal inoculation with 10^3 ffu of SARS-CoV-2 WA1/2020. (A) Mice were monitored for weight change for 7 days following viral infection. Mean weight change is shown. Error bars represent SEM. (B and C) At 7 dpi, nasal washes (B) and lungs (C) were collected, and viral RNA levels were determined. Median levels are shown; dotted line represents the limit of detection (LOD) of the assay. (D) A subset of the lungs from (C) were assessed for infectious virus by plaque assay. Median PFU/mL is shown. Dotted line indicates the LOD. (A–D) Data for each mAb are from two experiments; WEEV-204 (isotype control): n = 12; all other mAbs: n = 6 per group.

(E) SARS2-57 chimeric mouse Fv/human IgG1 Fc mAb was assayed for neutralization by FRNT against SARS-CoV-2 WA/2020. m, mouse hybridoma-derived mAb; h, recombinant chimeric mAb. Representative dose-response curves are shown from one of three experiments.

(F) hSARS2-57 N297Q mAb was assayed for binding to murine Fcγ receptors FcγRI and FcγRIV relative to intact hSARS2-57 by ELISA, using an anti-human capture mAb as a control. Shown is the mean relative absorbance obtained for N297Q over intact/WT mAb for each FcγR or capture mAb. Error bars represent SEM from three experiments.

(G and H) K18-hACE2 transgenic mice were administered 100 μg ($\sim$5 mg/kg) of the indicated chimeric mAb by intraperitoneal injection 24 h prior to intranasal inoculation with 10^3 ffu of SARS-CoV-2 WA1/2020. Data are from two experiments; hE16 (isotype control): n = 8 per group; hSARS2-57 and hSARS2-57 N297Q: n = 7 per group.

(I and J) K18-hACE2 transgenic mice were administered 200 μg (10 mg/kg) of the indicated mAb by intraperitoneal injection 24 h after intranasal inoculation with 10^3 ffu of SARS-CoV-2 WA1/2020. Data are from two experiments; hE16 (isotype control) and hSARS2-57: n = 6; hSARS2-57 N297Q: n = 5 per group.

(K and L) K18-hACE2 transgenic mice were administered 100 μg ($\sim$5 mg/kg) of the indicated mAb by intraperitoneal injection 24 h prior to intranasal inoculation with 10^3 ffu of SARS-CoV-2 WA1/2020 with sequence-confirmed wild-type furin cleavage site (FCS) sequence. Data are from two experiments; n = 12 per group.

(G, I, and K) Mean weight change is shown. Error bars represent SEM. (H, J, and L) At 7 dpi, lung, nasal washes, heart, and brain were collected and viral RNA levels were determined. (A, G, and I) One-way ANOVA of area under the curve of 4–7 dpi with Dunnet's post-test; (K) t test of area under the curve of 4–7 dpi; (B, C, H, and J) Kruskal-Wallis with Dunn's post-test; (D and L) Mann-Whitney test (ns, not significant, *$p < 0.05$, **$p < 0.01$, ***$p < 0.001$, ****$p < 0.0001$).
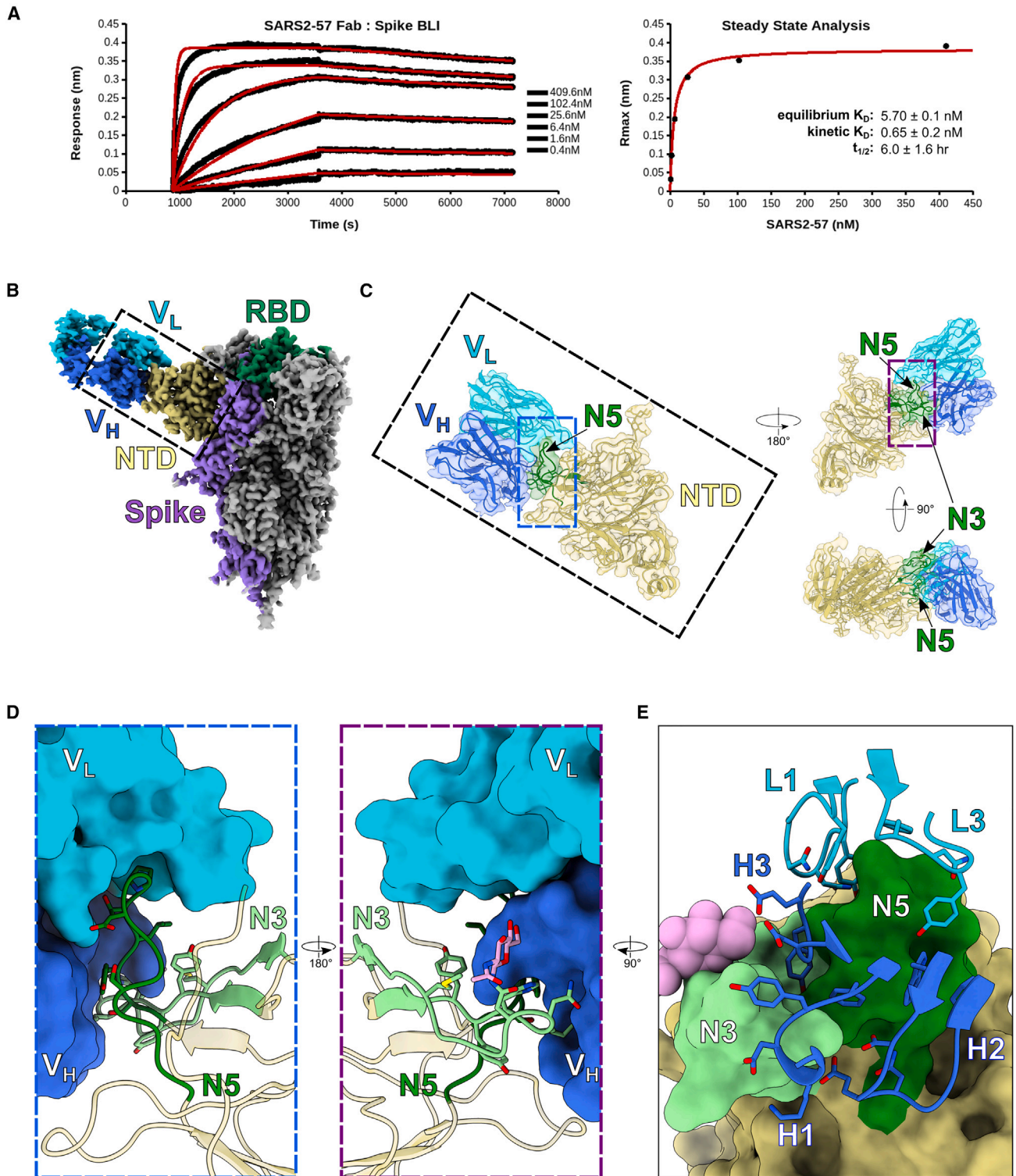
Figure 5. SARS2-57 binds NTD loops N3 and N5

(A) Biolayer interferometry signal (left) and steady-state analysis (right) of SARS2-57 Fab interacting with immobilized SARS-CoV-2 spike. Kinetic values were fitted to a global 1:1 binding model. Plots are representative of three technical replicates.

(legend continued on next page)

SARS2-57 binds NTD loops N3 and N5

To gain molecular insight into the basis for SARS2-57 protection, we first characterized the interaction of SARS-CoV-2 S with SARS2-57 antigen-binding fragments (Fab) using biolayer interferometry (BLI) (Figure 5A). SARS2-57 bound S with a remarkably long half-life ($t_{1/2}$ of 21,000 ± 5,900 s [6.0 ± 1.6 h]) and high monovalent affinity (kinetically derived K_D of 0.65 ± 0.2 nM). Steady-state analysis yielded an affinity estimate within an order of magnitude (equilibrium K_D of 5.7 ± 0.1 nM). We observed a slow on-rate with slight deviation from a 1:1 binding model, perhaps due to limited accessibility of the epitope.

To elucidate the structural basis for this interaction, we performed cryo-EM on complexes of SARS2-57 Fab and SARS-CoV-2 S protein (Figure S3; Table S1). We first generated two-dimensional classes and selected particles. We aligned these particles to a trimeric S reference model, performed C3 symmetry expansion, and then executed focused three-dimensional classification of a single NTD, identifying those with clear Fab density. To account for heterogeneity of Fab angle and NTD position relative to S, we performed a second round of whole-particle refinement with local angular sampling followed by focused three-dimensional classification of the NTD/Fv. The class with most clearly resolved Fv was then subjected to nonuniform refinement with local angular searches, generating a 3.13-Å map of trimeric S bound by a single Fab (Figures 5B, S4A, and S4C). While our structure depicts the spike with all RBDs down, this may be a product of symmetry expansion, as SARS2-57 does not impair engagement with ACE2 (Figure 1). Importantly, although the final map includes only one Fab per trimer, we can reasonably conclude that all three NTDs may be bound simultaneously without steric concerns.

To improve resolution at the binding interface, we performed local nonuniform refinement of the NTD/Fv, achieving a nominal resolution of 3.13 Å for this focused region (Figures 5C and S4D–S4F). The quality of the electron density map was such that we could unambiguously identify loops comprising the epitope and paratope with reasonable modeling of many side chains at the interface. SARS2-57 contacts two flexible loops on the side of the NTD, denoted N3 (residues 141–156) and N5 (residues 246–260)[38] (Figure 5C). Complementarity-determining regions (CDR) L1, L3, H2, and H3 of SARS2-57 form a pocket enveloping loop N5, with Y102 of CDR H3 inserted between N3 and N5. CDRs H1 and H2 likewise make additional contact with loop N3, creating a small additional pocket into which loop N3 protrudes (Figures 5D and 5E). CDR H3 rests proximal to an N149-linked glycan within loop N3 (Figure 5E), although this glycan is poorly ordered in our map. Altogether, this epitope

matches the previous description of an antigenic supersite including loops N3 and N5 (and N1 [residues 14–26]).[37,54] These findings also are consistent with the relatively slow association kinetics observed via BLI, as these loops may only occasionally adopt conformations competent to interact with SARS2-57 (Figure 5A).

To corroborate this structural model, we conducted independent epitope mapping via neutralization escape.[66] We passaged VSV-eGFP-SARS-CoV-2-S chimeric virus in the presence of SARS2-57 to select for resistant mutants, which were isolated and sequenced. We isolated VSV chimeric virus with mutations within NTD loops N3 (Y144C, K147 T/E/N, Y148-M153del) and N5 (Y248D, T250A, P251S/LH, and W258R) (Figures 6A and 6B). In addition, we performed hydrogen-deuterium exchange mass spectrometry (HDX-MS) with SARS2-57 and S protein. In accordance with our structural and escape mutant data, SARS2-57 binding protected peptides in loops N3 and N5, particularly peptides P139-H144 (which is likely protected via compression of loop N3 upon binding) and H245-G257 (which is directly contacted and shielded by mAb SARS2-57) (Figure S5).

SARS2-57 recognizes many SARS-CoV-2 variants

SARS-CoV-2 viral variants of concern (VOCs) and variants of interest (VOIs) harbor mutations in epitopes targeted by neutralizing mAbs, including in the NTD and RBD (Figure 6C). To further assess our structural model and evaluate direct binding of SARS2-57 to VOC/VOI S proteins, we stained cells infected with B.1.1.7, B.1.429, B.1.1.298. B.1.617.1, B.1.617.2, B.1.526, B.1.630, B.1.621, BA.1, BA.1.1, or BA.2 isolates, or chimeric WA1/2020 viruses expressing the S protein of B.1.351 (Wash-B.1.351) or B.1.1.28 (Wash-B.1.1.28).[32,49] SARS2-38, an mAb that recognizes a conserved epitope on the RBD, bound to cells infected with any of the variants except BA.1 or BA.1.1 (Figure 6D). SARS2-57 bound cells infected with most variants comparably to SARS2-38 (Figure 6D), including B.1.1.7, which features a Y144del (equivalent to Y145del in some S protein alignments); this finding was unexpected because Y144C was a neutralization escape mutant for SARS2-57 in the context of the VSV chimeric virus. In contrast, SARS2-57 failed to bind cells infected with Wash-B.1.351, B.1.630, BA.1, or BA.1.1 (Figure 6D), which may be due to the presence of deletions within the N3 loop (BA.1 and BA.1.1) or proximal to the N5 loop (Wash-B.1.351 and B.1.630).

Broad recognition and avid staining of variant spikes on infected cells suggests that SARS2-57 tolerates a variety of NTD mutations and could mediate Fc-effector functions against several variants. To further characterize the activity of SARS2-57 against variant viruses, we evaluated the neutralization potency of SARS2-57
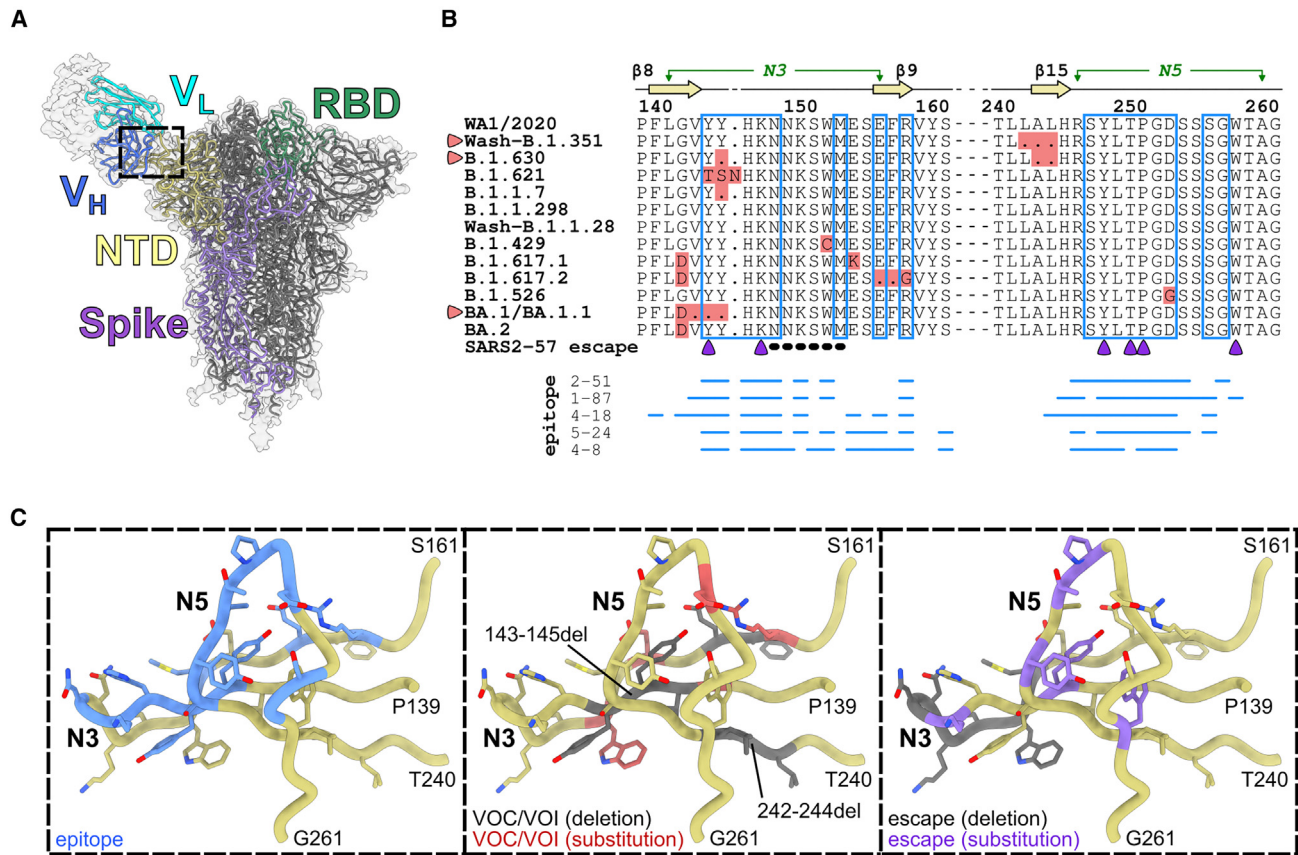
(B) Density map of SARS2-57 Fab bound to trimeric SARS-CoV-2 S with all RBDs in the down position. The NTD bound by SARS2-57 is shown in yellow, with the RBD of the same monomer colored green and the rest of the monomer shown in purple. The S trimer is otherwise colored gray. The SARS2-57 heavy and light chains are shown in royal blue and cyan, respectively.

(C) Magnified region from black box in (B). Focused density map of the Fv/NTD complex encompassing a refined atomic model. The NTD is shown in yellow, with loops N3 and N5 colored green. The SARS2-57 heavy and light chains are colored royal blue and cyan, respectively.

(D) Magnified regions from blue and purple boxes in (C), as indicated. A ribbon diagram of the NTD abutting a surface rendering of the SARS2-57 Fv. Loops N3 and N5 are colored mint and forest green, respectively, with glycan N149 colored pink. The SARS2-57 heavy and light chains are colored royal blue and cyan, respectively. PISA contact residues are shown as sticks.

(E) A ribbon diagram of the SARS2-57 complementarity-determining regions (CDR) overlying a surface rendering of the NTD. Loops N3 and N5 are colored mint and forest green, respectively, with glycan N149 colored pink and the rest of the NTD shown in yellow. CDRs of the SARS2-57 heavy and light chain are colored royal blue and cyan, respectively, with PISA paratope residues shown as sticks.

Figure 6. Identification of SARS2-57 escape mutations

(A and B) Neutralization escape mutants were isolated by passaging a VSV-eGFP-SARS-CoV-2-S chimeric virus (S from D614G strain) in the presence of SARS2-57. Wild-type and escape mutant viruses were tested for neutralization sensitivity to SARS2-57 by plaque assay. (A) Representative plaque assay images are shown. Data are representative of two experiments. (B) The locations of escape mutants are highlighted on the structure of the SARS-CoV-2 S protein (PDB: 7C2L). Spike is colored tan, the NTD is colored blue, and the RBD is colored green. Mutations on NTD loop N3 are highlighted in red, while mutations on NTD loop N5 are highlighted in orange.

(C) SARS-CoV-2 variants and their mutations in spike.

(D) Vero-TMPRSS2 cells were inoculated with the indicated SARS-CoV-2 strains. At 48 h after infection, cells were stained with mAb SARS2-38 (upper) or SARS2-57 (lower) at a concentration of 10, 1, or 0.1 μg/mL prior to analysis by flow cytometry. The percent of positively stained cells was determined after gating on staining with WEEV-204 (isotype control). Shown is the relative percent of positively stained cells (normalized to SARS2-38 staining at 10 μg/mL for each variant or a polyclonal mixture for Omicron subvariants) from two experiments. Error bars represent SEM.

Figure 7. The SARS2-57 epitope may be remodeled by deletions in emerging variants

(A) Density map and fitted model of SARS2-57 Fv bound to trimeric SARS-CoV-2 S with all RBDs in the down position. The NTD bound by SARS2-57 is shown in yellow, with the RBD of the same monomer colored green and the rest of the monomer shown in purple. The S trimer is otherwise colored gray. The SARS2-57 heavy and light chains are shown in royal blue and cyan, respectively.

(B) Multiple sequence alignment of the NTD loops N3 and N5 from WA1/2020 and SARS-CoV-2 VOCs/VOIs with the PISA binding footprint of SARS2-57 boxed in blue. VOC/VOI mutations are highlighted in red, and SARS2-57 escape mutations are designated with purple triangles (substitutions) or a dotted black line (deletion). Red triangles indicate variants that escape SARS2-57 recognition. Secondary structure annotation is displayed above the alignment in yellow with loops N3 and N5 noted in green.[38] The PISA binding footprints of previously described human anti-NTD mAbs are compared below the alignment as blue lines. Antibodies 2–51, 4–18, 5–24, and 4–8 also contact loop N1 (not pictured).[37] (C) Magnified region from the black box in (A) displaying only residues included in (B). NTD loops are displayed as round ribbons with residues of interest shown as sticks. Residues are color coded to indicate epitope residues identified by PISA (blue, left), VOC/VOI substitutions or deletions (red or gray, middle), and escape substitutions or deletions (purple or gray, right). VOCs represented include those listed in (B) (i.e., Wash-B.1.351, B.1.630, B.1.621, B.1.1.7, B.1.1.298, Wash-B.1.1.28, B.1.429, B.1.617.1, B.1.617.2, B.1.526, BA.1, BA.1.1, and BA.2).

against a subset of our variant panel, including D614G, B.1.1.7, Wash-B.1.351, B.1.526, B.1.429, B.1.1.298, B.1.617.1, BA.1, BA.1.1, and BA.2 (Figure S6). As expected, SARS2-57 neutralized D614G with similar potency to WA1/2020 (EC$_{50}$ of 65.8 vs. 73 ng/mL) and failed to neutralize Wash-B.1.351, BA.1, and BA.1.1, consistent with the loss of binding observed on cell staining. In contrast to our staining experiment, SARS2-57 failed to neutralize most other variants in our panel with the exception of B.1.526 (Iota; EC$_{50}$ of 30.0 ng/mL), suggesting that binding to S on the surface of infected cells does not correlate with requirements for neutralization.

The SARS2-57 epitope may be remodeled by deletions in SARS-CoV-2 variants

SARS2-57 stained the surface of cells infected with WA1/2020 or most variants tested in this study; it failed to stain cells infected

with Wash-B.1.351, B.1.630, BA.1, or BA.1.1. To elucidate the basis of this finding, we mapped the SARS2-57 epitope alongside proximal variant mutations within the NTD or, for comparison, escape mutations identified in our VSV-eGFP-SARS-CoV-2-S chimeric virus screen (Figure 7). Variants harbor mutations in both loops were contacted by SARS2-57. For example, variant B.1.1.7 harbors 145del on loop N3; B.1.617.2 likewise harbors a deletion within N3, 156-157del, as well as R158G (Figures 7B and 7C). Variants B.1.429, B.1.617.1, B.1.621, and BA.2 also harbor point mutations within N3, with B.1.621 also containing an insertion (146N ins). In contrast, loop N5 is relatively conserved in VOCs/VOIs, featuring only a single substitution in variant B.1.526. These observations notwithstanding, mAb SARS2-57 avidly stained cells infected with these variants comparably to those infected by WA1/2020 (Figure 6D), suggesting that these mutations do not completely abrogate binding.

In comparison, escape mutations were identified throughout loops N3 (Y144C, K147 T/E/N, and 148–153 del) and loop N5 (Y248D, T250A, P251 S/L/H, and W258R) (Figures 6A and 6B) in our screen, albeit mostly at residues distinct from those mutated within VOCs/VOIs. B.1.621 harbors substitution Y144T yet remains susceptible to SARS2-57 binding, suggesting that threonine is more tolerable than cysteine at this position. Various individual substitutions at K147 also were sufficient to confer resistance in our screen, suggesting that this residue is critical for binding. Indeed, K147 inserts deeply into a pocket formed by CDRs H1 and H2, forming 21 close contacts and accounting for 15.3% of the buried surface area (134.07/878.0 Å^2) at the mAb SARS2-57/NTD interface (Table S2). Other critical residues serving as points of escape in our screen include Y248 (seven close contacts; 12.3% of buried surface area; 108.3/878.0 Å^2) and P251 (17 close contacts; 13.3% of buried surface area; 116.7/878.0 Å^2) (Table S2). These three key contacts (K147, Y248, and P251) are perfectly conserved in our panel of variants. In contrast, SARS2-57 contact residues mutated within our VOC/VOI panel (including Y144, Y145, E156, R158, and D253) cumulatively account for 13.2% of the interface (115.7/878.0 Å^2), consistent with the antibody's ability to accommodate these alterations.

SARS2-57 failed to bind B.1.351 and B.1.630 S proteins on the surface of infected cells (Figure 6D). While SARS2-57 contact residues are highly conserved in these variants, both variants have deletions immediately upstream of loop N5 (242-244del for B.1.351 and 243-244del for B.1.630) (Figures 7B and 7C). SARS2-57 likewise failed to bind BA.1 or BA.1.1 S proteins, which share a deletion of residues 143–145, overlapping the SARS2-57 epitope in loop N3 (Figures 7B and 7C). Thus, VOCs/VOIs may evade NTD-directed antibodies through deletions within or proximal to the epitope, which retract or displace loops critical for binding. Remodeling of loops N3 and N5 likely confers resistance to many NTD supersite-directed antibodies (Figure 7B).[37,42,52,54]

An anti-RBD/anti-NTD mAb combination prevents generation of neutralization escape mutants

Resistant variants emerge rapidly during mAb monotherapy both *in vitro* and in the clinic,[67] highlighting a need for improved therapeutic strategies. Combinations of mAbs targeting different epitopes may prevent escape selection, as the virus must develop mutations at multiple locations to avoid recognition. We tested the ability of an antibody combination of anti-NTD mAb SARS2-57 and anti-RBD mAb SARS2-02 to prevent resistance following passage of VSV-eGFP-SARS-CoV-2-S chimeric virus in the presence of both antibodies in comparison with either mAb alone. Whereas viral escape mutants readily expanded in the presence of SARS2-57 or SARS2-02 alone, they were not detected when passaged in the presence of both SARS2-57/SARS2-02 mAbs (Figure S7).

DISCUSSION

The majority of neutralizing anti-SARS-CoV-2 S mAbs target the RBD and directly block ACE2 binding.[13–15,17–24,26–35,45,66] Fewer neutralizing mAbs targeting the NTD or domain S2 have been described, and their mechanism of action *in vitro* and *in vivo* is

poorly understood.[17,37–42,66] As SARS-CoV-2 variants with enhanced resistance to polyclonal sera and therapeutic mAbs continue to emerge,[9,12,49–53] it is critical to characterize the antigenicity of S protein in greater depth so that neutralizing antibodies targeting a variety of epitopes can be defined.

We generated and characterized extensively a panel of murine mAbs that bind non-RBD epitopes of SARS-CoV-2 S. We identified three competition groups, including mAbs that bind the NTD and compete with human mAb COV2-2676 (group 1), mAbs that bind the NTD but do not compete with COV2-2676 (group 2), and mAbs that bind non-NTD/non-RBD sites of the S protein (group 3). Some mAbs of each group inhibited infection of WA1/2020, though group 2 mAbs SARS2-11 and SARS2-29 and group 3 mAb SARS2-24 showed limited neutralizing activity (EC$_{50}$: >5 μg/mL). Group 1 mAb SARS2-57 was the most potently neutralizing (EC$_{50}$: 73 ng/mL), albeit with a resistant fraction that increased 2-fold in Vero-TMPRSS2 cells and nearly 4-fold in Vero-TMPRSS2-ACE2 cells compared with Vero E6 cells. The basis for this cell type-dependent resistant fraction is unclear, but it may indicate that host factors influence the threshold of neutralization by SARS2-57. SARS-CoV-2 entry into Vero E6 cells (without human ACE2) is thought to rely on a late endocytic/cathepsin-mediated pathway,[68] whereas Vero-TMPRSS2 and Vero-TMPRSS2-ACE2 cell lines are thought to favor viral fusion at the cell surface.[69] It is possible that the stoichiometric requirement for neutralization by SARS2-57 is less stringent for endosomal entry versus fusion at the cell surface, though this hypothesis warrants further study.

In contrast to many mAbs targeting the RBD, the non-RBD mAbs from our panel did not prevent ACE2 engagement or viral attachment to target cells, whereas some anti-NTD mAbs (SARS2-57 and SARS2-29) inhibited virus internalization by Vero E6 cells. Moreover, the non-RBD mAbs retained neutralization potency when administered post-attachment, with one anti-NTD mAb (SARS2-29) demonstrating greater potency. Thus, antibodies targeting the NTD or other non-RBD epitopes of SARS-CoV-2 S may block entry after attachment, and some NTD epitopes may be more accessible upon viral attachment. This property is consistent with the neutralization behavior of anti-NTD human mAbs.[42] The mechanism of post-attachment neutralization is unclear, but one anti-NTD mAb (SARS2-57) impaired S protein-mediated cell-cell fusion, consistent with previous descriptions of some NTD-specific mAbs.[54] These findings suggest that mAbs targeting the NTD may stabilize S in a fusion-incompetent conformation, as has been reported for the related Betacoronavirus MERS-CoV,[70] or alternatively block S2′ cleavage,[43] resulting in impaired viral fusion or cell-to-cell spread.

In addition to neutralizing infectious virions, an antibody may bind S on the cell surface and confer protection via Fc-effector functions.[28,42,57–61] In our panel, groups 2 and 3 mAbs negligibly stained infected cells, suggesting that some NTD and non-NTD/non-RBD epitopes are absent or obscured on the infected cell surface. In contrast, group 1 NTD-binding mAbs stained infected cells at higher levels than mAbs targeting the RBD. Accordingly, from the panel described in this study, only the group 1 mAb SARS2-57 conferred protection as prophylaxis in mice, and experiments with aglycosyl (N297Q) forms of SARS2-57 demonstrated a requirement of Fc-effector functions for *in vivo*

protective activity. This result contrasts with studies showing the Fc independence of highly neutralizing RBD-specific mAbs when administered as prophylaxis.[28,42,57–59]

SARS-CoV-2 continues to accumulate mutations that abrogate antibody binding to the RBD and NTD, including NTD mutations L18F (e.g., in B.1.1.28), Y145del (B.1.1.7), 242-244del (B.1.351), and 143-145del (BA.1 and BA1.1); some recurrent mutations, such as 69-70del (B.1.1.7 and B.1.1.298), may be associated with increased infectivity rather than antibody evasion.[71,72] The mutability of the NTD results in part from immune pressure on an antigenic supersite comprised roughly of three flexible loops denoted N1 (residues 14–26), N3 (residues 141–156), and N5 (residues 246–260).[37,54] Cryo-EM, escape mutant mapping, and HDX-MS confirmed that mAb SARS2-57 targets this site, primarily contacting loops N3 and N5. Despite the variability of these loops, SARS2-57 recognized many VOCs/VOIs in our panel. However, it failed to bind Wash-B.1.351 and variant B.1.630, likely due to 242-244del and 243-244del, respectively, as well as BA.1 and BA.1.1, which feature the 143-145del in loop N3. In B.1.351 S, 242-244del results in the inward dislocation of polar residues H245-R246-S247 in place of nonpolar residues L242-A243-L244. This causes a shift in the neighboring loop N3 and likely results in the retraction of loop N5, although N5 has not been resolved in available B.1.351 S structures.[73] In structural studies of BA.1 S, 143-145del has been shown to disorder the hairpin fold of loop N3.[74] These changes likely explain the impaired binding of mAb SARS2-57 to B.1.351, B.1.630, BA.1, and BA.1.1 S. Moreover, this antigenic remodeling may confer broad resistance to many neutralizing NTD-directed mAbs,[37,42,52,54,74] contributing to the reduced efficacy of ancestral S-based vaccines.[75–77] Some variants tested in our study (B.1.1.7, B.1.429, B.1.1.298, B.1.617.1, and BA.2) escaped neutralization by SARS2-57 despite being recognized on the surface of infected cells. The basis for this is unclear; it may be that nearby NTD mutations alter binding properties sufficiently to prevent neutralization, despite not abrogating the interaction altogether. Alternatively, mutations outside of the NTD (within S or elsewhere) may alter viral entry mechanics or kinetics, resulting in more stringent neutralization requirements for NTD-directed mAbs. As SARS-CoV-2 continues to evolve, it is critical that vaccines and mAb-based therapies target spatially distinct epitopes to minimize further resistance. As demonstrated in the present study, the virus can readily evade single mAbs targeting the NTD (SARS2-57) or RBD (SARS2-02), but the combination of two mAbs limits this escape.

Limitations of the study

We acknowledge limitations of our study. (1) While we show that SARS2-57 neutralizes SARS-CoV-2 post-attachment and can inhibit fusion, our experiments do not provide an exact mechanism by which SARS2-57 exerts these effects, nor do they explain the existence of the neutralization-resistant fraction. (2) We evaluated variant recognition by SARS2-57 via the staining of infected cells rather than quantitative kinetic experiments (e.g., BLI) that could detect changes in binding with greater sensitivity. (3) While we speculate how SARS2-57 might accommodate certain mutations found in viral variants, we have not directly characterized the binding of variants structurally. (4) We show that SARS2-57 recognizes certain viral variants on

the cell surface despite losing neutralization potency, but we did not evaluate *in vivo* whether SARS2-57 confers Fc-mediated protection against these variants.

In summary, we generated a panel of anti-SARS-CoV-2 mAbs targeting the spike NTD or other non-RBD epitopes, characterized their mechanism of action, and determined the structure of SARS-CoV-2 S bound to SARS2-57, a neutralizing and protective anti-NTD mAb. The epitope of SARS2-57 is an antigenic supersite targeted also by human mAbs and is highly mutable. Nevertheless, SARS2-57 recognizes most VOCs/VOIs tested in this study, albeit with diminished neutralizing activity. As escape from SARS2-57 is prevented by the addition of an anti-RBD mAb, combination therapy with anti-NTD and anti-RBD seems plausible as a therapeutic strategy.

STAR★METHODS

Detailed methods are provided in the online version of this paper and include the following:

- KEY RESOURCES TABLE
- RESOURCE AVAILABILITY
  - Lead contact
  - Materials availability
  - Data and code availability
- EXPERIMENTAL MODEL AND PARTICIPANT DETAILS
  - Cells
  - Viruses
  - Mouse studies
- METHOD DETAILS
  - Proteins
  - MAb generation
  - NTD-binding ELISA
  - Competition-binding analysis
  - Human ACE2 binding inhibition analysis
  - VSV-eGFP-SARS-CoV-2-S escape mutants
  - Determination of mAb concentration in hybridoma supernatant
  - Neutralization assay
  - Pre- and post-attachment neutralization assays
  - Attachment inhibition assay
  - Virus internalization assay
  - Syncytia formation assay
  - Anti-SARS-CoV-2 mAb binding to the surface of infected cells
  - Sequencing, cloning, and expression of chimeric IgG1
  - Measurement of viral burden and cytokine and chemokine levels
  - Binding analysis via biolayer interferometry
  - Cryo-EM sample preparation
  - Cryo-EM data collection
  - Cryo-EM data processing
  - Model building
  - Hydrogen-deuterium exchange (HDX) mass spectrometry peptide mapping
  - Epitope mapping by HDX
  - HDX data analysis
- QUANTIFICATION AND STATISTICAL ANALYSES

AUTHOR CONTRIBUTIONS

Conceptualization and methodology, L.J.A., L.A.V, M.S.D., D.H.F., Z.L., and S.P.J.W.; investigation, L.J.A., L.A.V., Z.L., P.G., R.E.C., S.R., B.M.W., S.S., and P.N.J.; key reagents, H.Z.; supervision and funding, D.H.F., M.S.D., S.P.J.W., J.E.C., and M.L.G.; writing – original draft, L.J.A., L.A.V., M.S.D., and D.H.F.; writing – review and editing, all authors.

DECLARATION OF INTERESTS

M.S.D. is a consultant for Inbios, Vir Biotechnology, Ocugen, Topspin Therapeutics, GlaxoSmithKline, Moderna, and Immunome. The Diamond laboratory has received unrelated funding support in sponsored research agreements from Vir Biotechnology, Emergent BioSolutions, and Moderna. Some of the mAbs described in this study have been licensed by Washington University to Bio X Cell. D.H.F. is a founder of Courier Therapeutics and has received funding support in a sponsored research agreement from Emergent BioSolutions. J.E.C. has served as a consultant for Eli Lilly and Luna Biologics, is a member of the Scientific Advisory Boards of CompuVax and Meissa Vaccines, and is the founder of IDBiologics. The Crowe laboratory at Vanderbilt University Medical Center has received sponsored research agreements from AstraZeneca and IDBiologics.

REFERENCES

1. Baden, L.R., El Sahly, H.M., Essink, B., Kotloff, K., Frey, S., Novak, R., Diemert, D., Spector, S.A., Rouphael, N., Creech, C.B., et al. (2021). Efficacy and Safety of the mRNA-1273 SARS-CoV-2 Vaccine. N. Engl. J. Med. *384*, 403–416.

2. Cathcart, A.L., Havenar-Daughton, C., Lempp, F.A., Ma, D., Schmid, M.A., Agostini, M.L., Guarino, B., Iulio, J.D., Rosen, L.E., Tucker, H., et al. (2021). The dual function monoclonal antibodies VIR-7831 and VIR-7832 demonstrate potent in Vitro and in Vivo activity against SARS-CoV-2. Preprint at bioRxiv. 2021.03.09.434607.

3. Chen, P., Nirula, A., Heller, B., Gottlieb, R.L., Boscia, J., Morris, J., Huhn, G., Cardona, J., Mocherla, B., Stosor, V., et al. (2021). SARS-CoV-2 Neutralizing Antibody LY-CoV555 in Outpatients with Covid-19. N. Engl. J. Med. *384*, 229–237.

4. Keech, C., Albert, G., Cho, I., Robertson, A., Reed, P., Neal, S., Plested, J.S., Zhu, M., Cloney-Clark, S., Zhou, H., et al. (2020). Phase 1-2 Trial of a SARS-CoV-2 Recombinant Spike Protein Nanoparticle Vaccine. N. Engl. J. Med. *383*, 2320–2332.

5. Polack, F.P., Thomas, S.J., Kitchin, N., Absalon, J., Gurtman, A., Lockhart, S., Perez, J.L., Pérez Marc, G., Moreira, E.D., Zerbini, C., et al. (2020). Safety and Efficacy of the BNT162b2 mRNA Covid-19 Vaccine. N. Engl. J. Med. *383*, 2603–2615.

6. Sadoff, J., Le Gars, M., Shukarev, G., Heerwegh, D., Truyers, C., de Groot, A.M., Stoop, J., Tete, S., Van Damme, W., Leroux-Roels, I., et al. (2021). Interim Results of a Phase 1-2a Trial of Ad26.COV2.S Covid-19 Vaccine. N. Engl. J. Med. *384*, 1824–1835.

7. Voysey, M., Clemens, S.A.C., Madhi, S.A., Weckx, L.Y., Folegatti, P.M., Aley, P.K., Angus, B., Baillie, V.L., Barnabas, S.L., Bhorat, Q.E., et al. (2021). Safety and efficacy of the ChAdOx1 nCoV-19 vaccine (AZD1222) against SARS-CoV-2: an interim analysis of four randomised controlled trials in Brazil, South Africa, and the UK. Lancet *397*, 99–111.

8. Weinreich, D.M., Sivapalasingam, S., Norton, T., Ali, S., Gao, H., Bhore, R., Musser, B.J., Soo, Y., Rofail, D., Im, J., et al. (2021). REGN-COV2, a Neutralizing Antibody Cocktail, in Outpatients with Covid-19. N. Engl. J. Med. *384*, 238–251.

9. Chen, R.E., Winkler, E.S., Case, J.B., Aziati, I.D., Bricker, T.L., Joshi, A., Darling, T.L., Ying, B., Errico, J.M., Shrihari, S., et al. (2021). In vivo monoclonal antibody efficacy against SARS-CoV-2 variant strains. Nature *596*, 103–108.

10. Zhou, H., Dcosta, B.M., Landau, N.R., and Tada, T. (2022). Resistance of SARS-CoV-2 Omicron BA.1 and BA.2 Variants to Vaccine-Elicited Sera and Therapeutic Monoclonal Antibodies. Viruses *14*, 1334.

11. Wang, Q., Guo, Y., Iketani, S., Nair, M.S., Li, Z., Mohri, H., Wang, M., Yu, J., Bowen, A.D., Chang, J.Y., et al. (2022). Antibody evasion by SARS-CoV-2 Omicron subvariants BA.2.12.1, BA.4 and BA.5. Nature *608*, 603–608.

12. Wang, Q., Iketani, S., Li, Z., Liu, L., Guo, Y., Huang, Y., Bowen, A.D., Liu, M., Wang, M., Yu, J., et al. (2023). Alarming antibody evasion properties of rising SARS-CoV-2 BQ and XBB subvariants. Cell *186*, 279–286.e8.

13. Alsoussi, W.B., Turner, J.S., Case, J.B., Zhao, H., Schmitz, A.J., Zhou, J.Q., Chen, R.E., Lei, T., Rizk, A.A., McIntire, K.M., et al. (2020). A Potently Neutralizing Antibody Protects Mice against SARS-CoV-2 Infection. J. Immunol. *205*, 915–922.

14. Barnes, C.O., Jette, C.A., Abernathy, M.E., Dam, K.-M.A., Esswein, S.R., Gristick, H.B., Malyutin, A.G., Sharaf, N.G., Huey-Tubman, K.E., Lee, Y.E., et al. (2020). SARS-CoV-2 neutralizing antibody structures inform therapeutic strategies. Nature *588*, 682–687.

15. Barnes, C.O., West, A.P., Huey-Tubman, K.E., Hoffmann, M.A.G., Sharaf, N.G., Hoffman, P.R., Koranda, N., Gristick, H.B., Gaebler, C., Muecksch, F., et al. (2020). Structures of Human Antibodies Bound to SARS-CoV-2 Spike Reveal Common Epitopes and Recurrent Features of Antibodies. Cell *182*, 828–842.e16.

16. Baum, A., Ajithdoss, D., Copin, R., Zhou, A., Lanza, K., Negron, N., Ni, M., Wei, Y., Mohammadi, K., Musser, B., et al. (2020). REGN-COV2 antibodies prevent and treat SARS-CoV-2 infection in rhesus macaques and hamsters. Science *370*, 1110–1115.

17. Brouwer, P.J.M., Caniels, T.G., van der Straten, K., Snitselaar, J.L., Aldon, Y., Bangaru, S., Torres, J.L., Okba, N.M.A., Claireaux, M., Kerster, G., et al. (2020). Potent neutralizing antibodies from COVID-19 patients define multiple targets of vulnerability. Science *369*, 643–650.

18. Cao, Y., Su, B., Guo, X., Sun, W., Deng, Y., Bao, L., Zhu, Q., Zhang, X., Zheng, Y., Geng, C., et al. (2020). Potent Neutralizing Antibodies against SARS-CoV-2 Identified by High-Throughput Single-Cell Sequencing of Convalescent Patients' B Cells. Cell *182*, 73–84.e16.

19. Fagre, A.C., Manhard, J., Adams, R., Eckley, M., Zhan, S., Lewis, J., Rocha, S.M., Woods, C., Kuo, K., Liao, W., et al. (2020). A Potent SARS-CoV-2 Neutralizing Human Monoclonal Antibody That Reduces Viral Burden and Disease Severity in Syrian Hamsters. Front. Immunol. *11*, 614256.

20. Hansen, J., Baum, A., Pascal, K.E., Russo, V., Giordano, S., Wloga, E., Fulton, B.O., Yan, Y., Koon, K., Patel, K., et al. (2020). Studies in humanized mice and convalescent humans yield a SARS-CoV-2 antibody cocktail. Science *369*, 1010–1014.

21. Hassan, A.O., Case, J.B., Winkler, E.S., Thackray, L.B., Kafai, N.M., Bailey, A.L., McCune, B.T., Fox, J.M., Chen, R.E., Alsoussi, W.B., et al. (2020). A SARS-CoV-2 Infection Model in Mice Demonstrates Protection by Neutralizing Antibodies. Cell *182*, 744–753.e4.

22. Hurlburt, N.K., Seydoux, E., Wan, Y.-H., Edara, V.V., Stuart, A.B., Feng, J., Suthar, M.S., McGuire, A.T., Stamatatos, L., and Pancera, M. (2020). Structural basis for potent neutralization of SARS-CoV-2 and role of antibody affinity maturation. Nat. Commun. *11*, 5413.

23. Kreye, J., Reincke, S.M., Kornau, H.-C., Sánchez-Sendin, E., Corman, V.M., Liu, H., Yuan, M., Wu, N.C., Zhu, X., Lee, C.-C.D., et al. (2020). A Therapeutic Non-self-reactive SARS-CoV-2 Antibody Protects from Lung Pathology in a COVID-19 Hamster Model. Cell *183*, 1058–1069.e19.

24. Li, W., Chen, C., Drelich, A., Martinez, D.R., Gralinski, L.E., Sun, Z., Schäfer, A., Kulkarni, S.S., Liu, X., Leist, S.R., et al. (2020). Rapid identification of a human antibody with high prophylactic and therapeutic efficacy in three animal models of SARS-CoV-2 infection. Proc. Natl. Acad. Sci. USA *117*, 29832–29838.

25. Liu, L., Wang, P., Nair, M.S., Yu, J., Rapp, M., Wang, Q., Luo, Y., Chan, J.F.-W., Sahi, V., Figueroa, A., et al. (2020). Potent neutralizing antibodies against multiple epitopes on SARS-CoV-2 spike. Nature *584*, 450–456.

26. Lv, Z., Deng, Y.-Q., Ye, Q., Cao, L., Sun, C.-Y., Fan, C., Huang, W., Sun, S., Sun, Y., Zhu, L., et al. (2020). Structural basis for neutralization of SARS-CoV-2 and SARS-CoV by a potent therapeutic antibody. Science *369*, 1505–1509.

27. Rogers, T.F., Zhao, F., Huang, D., Beutler, N., Burns, A., He, W.-T., Limbo, O., Smith, C., Song, G., Woehl, J., et al. (2020). Isolation of potent SARS-CoV-2 neutralizing antibodies and protection from disease in a small animal model. Science *369*, 956–963.

28. Schäfer, A., Muecksch, F., Lorenzi, J.C.C., Leist, S.R., Cipolla, M., Bournazos, S., Schmidt, F., Maison, R.M., Gazumyan, A., Martinez, D.R., et al. (2021). Antibody potency, effector function, and combinations in protection and therapy for SARS-CoV-2 infection in vivo. J. Exp. Med. *218*, e20201993.

29. Seydoux, E., Homad, L.J., MacCamy, A.J., Parks, K.R., Hurlburt, N.K., Jennewein, M.F., Akins, N.R., Stuart, A.B., Wan, Y.-H., Feng, J., et al. (2020). Analysis of a SARS-CoV-2-Infected Individual Reveals Development of Potent Neutralizing Antibodies with Limited Somatic Mutation. Immunity *53*, 98–105.e5.

30. Shi, R., Shan, C., Duan, X., Chen, Z., Liu, P., Song, J., Song, T., Bi, X., Han, C., Wu, L., et al. (2020). A human neutralizing antibody targets the receptor-binding site of SARS-CoV-2. Nature *584*, 120–124.

31. Tortorici, M.A., Beltramello, M., Lempp, F.A., Pinto, D., Dang, H.V., Rosen, L.E., McCallum, M., Bowen, J., Minola, A., Jaconi, S., et al. (2020). Ultrapotent human antibodies protect against SARS-CoV-2 challenge via multiple mechanisms. Science *370*, 950–957.

32. VanBlargan, L.A., Adams, L.J., Liu, Z., Chen, R.E., Gilchuk, P., Raju, S., Smith, B.K., Zhao, H., Case, J.B., Winkler, E.S., et al. (2021). A potently neutralizing SARS-CoV-2 antibody inhibits variants of concern by utilizing unique binding residues in a highly conserved epitope. Immunity *54*, 2399–2416.e6.

33. Wec, A.Z., Wrapp, D., Herbert, A.S., Maurer, D.P., Haslwanter, D., Sakharkar, M., Jangra, R.K., Dieterle, M.E., Lilov, A., Huang, D., et al. (2020). Broad neutralization of SARS-related viruses by human monoclonal antibodies. Science *369*, 731–736.

34. Wu, N.C., Yuan, M., Liu, H., Lee, C.-C.D., Zhu, X., Bangaru, S., Torres, J.L., Caniels, T.G., Brouwer, P.J.M., van Gils, M.J., et al. (2020). An Alternative Binding Mode of IGHV3-53 Antibodies to the SARS-CoV-2 Receptor Binding Domain. Cell Rep. *33*, 108274.

35. Zost, S.J., Gilchuk, P., Case, J.B., Binshtein, E., Chen, R.E., Nkolola, J.P., Schäfer, A., Reidy, J.X., Trivette, A., Nargi, R.S., et al. (2020). Potently neutralizing and protective human antibodies against SARS-CoV-2. Nature *584*, 443–449.

36. Errico, J.M., Zhao, H., Chen, R.E., Liu, Z., Case, J.B., Ma, M., Schmitz, A.J., Rau, M.J., Fitzpatrick, J.A.J., Shi, P.-Y., et al. (2021). Structural mechanism of SARS-CoV-2 neutralization by two murine antibodies targeting the RBD. Cell Rep. *37*, 109881.

37. Cerutti, G., Guo, Y., Zhou, T., Gorman, J., Lee, M., Rapp, M., Reddem, E.R., Yu, J., Bahna, F., Bimela, J., et al. (2021). Potent SARS-CoV-2 neutralizing antibodies directed against spike N-terminal domain target a single supersite. Cell Host Microbe *29*, 819–833.e7.

38. Chi, X., Yan, R., Zhang, J., Zhang, G., Zhang, Y., Hao, M., Zhang, Z., Fan, P., Dong, Y., Yang, Y., et al. (2020). A neutralizing human antibody binds to the N-terminal domain of the Spike protein of SARS-CoV-2. Science *369*, 650–655.

39. Ng, K.W., Faulkner, N., Cornish, G.H., Rosa, A., Harvey, R., Hussain, S., Ulferts, R., Earl, C., Wrobel, A.G., Benton, D.J., et al. (2020). Preexisting and de novo humoral immunity to SARS-CoV-2 in humans. Science *370*, 1339–1343.

40. Pinto, D., Sauer, M.M., Czudnochowski, N., Low, J.S., Tortorici, M.A., Housley, M.P., Noack, J., Walls, A.C., Bowen, J.E., Guarino, B., et al. (2021). Broad betacoronavirus neutralization by a stem helix-specific human antibody. Science *373*, 1109–1116. eabj3321.

41. Song, G., He, W.T., Callaghan, S., Anzanello, F., Huang, D., Ricketts, J., Torres, J.L., Beutler, N., Peng, L., Vargas, S., et al. (2021). Cross-reactive serum and memory B-cell responses to spike protein in SARS-CoV-2 and endemic coronavirus infection. Nat. Commun. *12*, 2938.

42. Suryadevara, N., Shrihari, S., Gilchuk, P., VanBlargan, L.A., Binshtein, E., Zost, S.J., Nargi, R.S., Sutton, R.E., Winkler, E.S., Chen, E.C., et al. (2021). Neutralizing and protective human monoclonal antibodies recognizing the N-terminal domain of the SARS-CoV-2 spike protein. Cell *184*, 2316–2331.e15.

43. Qing, E., Li, P., Cooper, L., Schulz, S., Jäck, H.M., Rong, L., Perlman, S., and Gallagher, T. (2022). Inter-domain communication in SARS-CoV-2 spike proteins controls protease-triggered cell entry. Cell Rep. *39*, 110786.

44. Suryadevara, N., Shiakolas, A.R., VanBlargan, L.A., Binshtein, E., Chen, R.E., Case, J.B., Kramer, K.J., Armstrong, E.C., Myers, L., Trivette, A., et al. (2022). An antibody targeting the N-terminal domain of SARS-CoV-2 disrupts the spike trimer. J. Clin. Invest. *132*, e159062.

45. Baum, A., Fulton, B.O., Wloga, E., Copin, R., Pascal, K.E., Russo, V., Giordano, S., Lanza, K., Negron, N., Ni, M., et al. (2020). Antibody cocktail to SARS-CoV-2 spike protein prevents rapid mutational escape seen with individual antibodies. Science *369*, 1014–1018.

46. Greaney, A.J., Starr, T.N., Gilchuk, P., Zost, S.J., Binshtein, E., Loes, A.N., Hilton, S.K., Huddleston, J., Eguia, R., Crawford, K.H.D., et al. (2021). Complete Mapping of Mutations to the SARS-CoV-2 Spike Receptor-Binding Domain that Escape Antibody Recognition. Cell Host Microbe *29*, 44–57.e9.

47. Greaney, A.J., Loes, A.N., Crawford, K.H.D., Starr, T.N., Malone, K.D., Chu, H.Y., and Bloom, J.D. (2021). Comprehensive mapping of mutations in the SARS-CoV-2 receptor-binding domain that affect recognition by polyclonal human plasma antibodies. Cell Host Microbe *29*, 463–476.e6.

48. Starr, T.N., Greaney, A.J., Dingens, A.S., and Bloom, J.D. (2021). Complete map of SARS-CoV-2 RBD mutations that escape the monoclonal antibody LY-CoV555 and its cocktail with LY-CoV016. Cell Rep. Med. *2*, 100255.

49. Chen, R.E., Zhang, X., Case, J.B., Winkler, E.S., Liu, Y., VanBlargan, L.A., Liu, J., Errico, J.M., Xie, X., Suryadevara, N., et al. (2021). Resistance of SARS-CoV-2 variants to neutralization by monoclonal and serum-derived polyclonal antibodies. Nat. Med. *27*, 717–726.

50. Hoffmann, M., Arora, P., Groß, R., Seidel, A., Hörnich, B.F., Hahn, A.S., Krüger, N., Graichen, L., Hofmann-Winkler, H., Kempf, A., et al. (2021). SARS-CoV-2 variants B.1.351 and P.1 escape from neutralizing antibodies. Cell *184*, 2384–2393.e12.

51. Thomson, E.C., Rosen, L.E., Shepherd, J.G., Spreafico, R., da Silva Filipe, A., Wojcechowskyj, J.A., Davis, C., Piccoli, L., Pascall, D.J., Dillen, J., et al. (2021). Circulating SARS-CoV-2 spike N439K variants maintain fitness while evading antibody-mediated immunity. Cell *184*, 1171–1187.e20.

52. Wang, P., Nair, M.S., Liu, L., Iketani, S., Luo, Y., Guo, Y., Wang, M., Yu, J., Zhang, B., Kwong, P.D., et al. (2021). Antibody resistance of SARS-CoV-2 variants B.1.351 and B.1.1.7. Nature 593, 130–135.

53. Weisblum, Y., Schmidt, F., Zhang, F., DaSilva, J., Poston, D., Lorenzi, J.C., Muecksch, F., Rutkowska, M., Hoffmann, H.-H., Michailidis, E., et al. (2020). Escape from neutralizing antibodies by SARS-CoV-2 spike protein variants. Elife 9, e61312.

54. McCallum, M., De Marco, A., Lempp, F.A., Tortorici, M.A., Pinto, D., Walls, A.C., Beltramello, M., Chen, A., Liu, Z., Zatta, F., et al. (2021). N-terminal domain antigenic mapping reveals a site of vulnerability for SARS-CoV-2. Cell 184, 2332–2347.e16.

55. Yuan, M., Wu, N.C., Zhu, X., Lee, C.-C.D., So, R.T.Y., Lv, H., Mok, C.K.P., and Wilson, I.A. (2020). A highly conserved cryptic epitope in the receptor binding domains of SARS-CoV-2 and SARS-CoV. Science 368, 630–633.

56. Meng, B., Abdullahi, A., Ferreira, I.A.T.M., Goonawardane, N., Saito, A., Kimura, I., Yamasoba, D., Gerber, P.P., Fatihi, S., Rathore, S., et al. (2022). Altered TMPRSS2 usage by SARS-CoV-2 Omicron impacts infectivity and fusogenicity. Nature 603, 706–714.

57. Chan, C.E.Z., Seah, S.G.K., Chye, D.H., Massey, S., Torres, M., Lim, A.P.C., Wong, S.K.K., Neo, J.J.Y., Wong, P.S., Lim, J.H., et al. (2021). The Fc-mediated effector functions of a potent SARS-CoV-2 neutralizing antibody, SC31, isolated from an early convalescent COVID-19 patient, are essential for the optimal therapeutic efficacy of the antibody. PLoS One 16, e0253487.

58. Gorman, M.J., Patel, N., Guebre-Xabier, M., Zhu, A., Atyeo, C., Pullen, K.M., Loos, C., Goez-Gazi, Y., Carrion, R., Tian, J.-H., et al. (2021). Collaboration between the Fab and Fc contribute to maximal protection against SARS-CoV-2 in nonhuman primates following NVX-CoV2373 Subunit Vaccine with Matrix-M™ Vaccination. Preprint at bioRxiv. 2021.02.05.429759.

59. Winkler, E.S., Gilchuk, P., Yu, J., Bailey, A.L., Chen, R.E., Chong, Z., Zost, S.J., Jang, H., Huang, Y., Allen, J.D., et al. (2021). Human neutralizing antibodies against SARS-CoV-2 require intact Fc effector functions for optimal therapeutic protection. Cell 184, 1804–1820.e16.

60. Mackin, S.R., Desai, P., Whitener, B.M., Karl, C.E., Liu, M., Baric, R.S., Edwards, D.K., Chicz, T.M., McNamara, R.P., Alter, G., and Diamond, M.S. (2023). Fc-γR-dependent antibody effector functions are required for vaccine-mediated protection against antigen-shifted variants of SARS-CoV-2. Nat. Microbiol. 8, 569–580.

61. Case, J.B., Mackin, S., Errico, J.M., Chong, Z., Madden, E.A., Whitener, B., Guarino, B., Schmid, M.A., Rosenthal, K., Ren, K., et al. (2022). Resilience of S309 and AZD7442 monoclonal antibody treatments against infection by SARS-CoV-2 Omicron lineage strains. Nat. Commun. 13, 3824.

62. Winkler, E.S., Bailey, A.L., Kafai, N.M., Nair, S., McCune, B.T., Yu, J., Fox, J.M., Chen, R.E., Earnest, J.T., Keeler, S.P., et al. (2020). SARS-CoV-2 infection of human ACE2-transgenic mice causes severe lung inflammation and impaired function. Nat. Immunol. 21, 1327–1335.

63. Dekkers, G., Bentlage, A.E.H., Stegmann, T.C., Howie, H.L., Lissenberg-Thunnissen, S., Zimring, J., Rispens, T., and Vidarsson, G. (2017). Affinity of human IgG subclasses to mouse Fc gamma receptors. mAbs 9, 767–773.

64. Tao, M.-H., and Morrison, S.L. (1989). Studies of aglycosylated chimeric mouse-human IgG. Role of carbohydrate in the structure and effector functions mediated by the human IgG constant region. J. Immunol. 143, 2595–2601.

65. Johnson, B.A., Xie, X., Bailey, A.L., Kalveram, B., Lokugamage, K.G., Muruato, A., Zou, J., Zhang, X., Juelich, T., Smith, J.K., et al. (2021). Loss of furin cleavage site attenuates SARS-CoV-2 pathogenesis. Nature 591, 293–299. https://doi.org/10.1038/s41586-021-03237-4.

66. Liu, Z., VanBlargan, L.A., Bloyet, L.-M., Rothlauf, P.W., Chen, R.E., Stumpf, S., Zhao, H., Errico, J.M., Theel, E.S., Liebeskind, M.J., et al. (2021). Identification of SARS-CoV-2 spike mutations that attenuate

monoclonal and serum antibody neutralization. Cell Host Microbe 29, 477–488.e4.

67. Choudhary, M.C., Chew, K.W., Deo, R., Flynn, J.P., Regan, J., Crain, C.R., Moser, C., Hughes, M.D., Ritz, J., Ribeiro, R.M., et al. (2022). Emergence of SARS-CoV-2 escape mutations during Bamlanivimab therapy in a phase II randomized clinical trial. Nat. Microbiol. 7, 1906–1917.

68. Kang, Y.-L., Chou, Y.Y., Rothlauf, P.W., Liu, Z., Soh, T.K., Cureton, D., Case, J.B., Chen, R.E., Diamond, M.S., Whelan, S.P.J., and Kirchhausen, T. (2020). Inhibition of PIKfyve kinase prevents infection by Zaire ebolavirus and SARS-CoV-2. Proc. Natl. Acad. Sci. USA 117, 20803–20813.

69. Hoffmann, M., Kleine-Weber, H., Schroeder, S., Krüger, N., Herrler, T., Erichsen, S., Schiergens, T.S., Herrler, G., Wu, N.-H., Nitsche, A., et al. (2020). SARS-CoV-2 Cell Entry Depends on ACE2 and TMPRSS2 and Is Blocked by a Clinically Proven Protease Inhibitor. Cell 181, 271–280.e8.

70. Zhou, H., Chen, Y., Zhang, S., Niu, P., Qin, K., Jia, W., Huang, B., Zhang, S., Lan, J., Zhang, L., et al. (2019). Structural definition of a neutralization epitope on the N-terminal domain of MERS-CoV spike glycoprotein. Nat. Commun. 10, 3068.

71. Harvey, W.T., Carabelli, A.M., Jackson, B., Gupta, R.K., Thomson, E.C., Harrison, E.M., Ludden, C., Reeve, R., Rambaut, A., et al.; COVID-19 Genomics UK COG-UK Consortium (2021). SARS-CoV-2 variants, spike mutations and immune escape. Nat. Rev. Microbiol. 19, 409–424.

72. Plante, J.A., Mitchell, B.M., Plante, K.S., Debbink, K., Weaver, S.C., and Menachery, V.D. (2021). The variant gambit: COVID-19's next move. Cell Host Microbe 29, 508–515.

73. Cai, Y., Zhang, J., Xiao, T., Lavine, C.L., Rawson, S., Peng, H., Zhu, H., Anand, K., Tong, P., Gautam, A., et al. (2021). Structural basis for enhanced infectivity and immune evasion of SARS-CoV-2 variants. Science 373, 642–648.

74. Cui, Z., Liu, P., Wang, N., Wang, L., Fan, K., Zhu, Q., Wang, K., Chen, R., Feng, R., Jia, Z., et al. (2022). Structural and functional characterizations of infectivity and immune evasion of SARS-CoV-2 Omicron. Cell 185, 860–871.e13.

75. Madhi, S.A., Baillie, V., Cutland, C.L., Voysey, M., Koen, A.L., Fairlie, L., Padayachee, S.D., Dheda, K., Barnabas, S.L., Bhorat, Q.E., et al. (2021). Efficacy of the ChAdOx1 nCoV-19 Covid-19 Vaccine against the B.1.351 Variant. N. Engl. J. Med. 384, 1885–1898.

76. Planas, D., Bruel, T., Grzelak, L., Guivel-Benhassine, F., Staropoli, I., Porrot, F., Planchais, C., Buchrieser, J., Rajah, M.M., Bishop, E., et al. (2021). Sensitivity of infectious SARS-CoV-2 B.1.1.7 and B.1.351 variants to neutralizing antibodies. Nat. Med. 27, 917–924.

77. Shen, X., Tang, H., Pajon, R., Smith, G., Glenn, G.M., Shi, W., Korber, B., and Montefiori, D.C. (2021). Neutralization of SARS-CoV-2 Variants B.1.429 and B.1.351. N. Engl. J. Med. 384, 2352–2354.

78. ter Meulen, J., van den Brink, E.N., Poon, L.L., Marissen, W.E., Leung, C.S., Cox, F., Cheung, C.Y., Bakker, A.Q., Bogaards, J.A., van Deventer, E., et al. (2006). Human monoclonal antibody combination against SARS coronavirus: synergy and coverage of escape mutants. PLoS Med 3, e237. https://doi.org/10.1371/journal.pmed.0030237.

79. Case, J.B., Bailey, A.L., Kim, A.S., Chen, R.E., and Diamond, M.S. (2020). Growth, detection, quantification, and inactivation of SARS-CoV-2. Virology 548, 39–48.

80. Zheng, S.Q., Palovcak, E., Armache, J.-P., Verba, K.A., Cheng, Y., and Agard, D.A. (2017). MotionCor2: anisotropic correction of beam-induced motion for improved cryo-electron microscopy. Nat. Methods 14, 331–332.

81. Zhang, K. (2016). Gctf: Real-time CTF determination and correction. J. Struct. Biol. 193, 1–12.

82. Wagner, T., Merino, F., Stabrin, M., Moriya, T., Antoni, C., Apelbaum, A., Hagel, P., Sitsel, O., Raisch, T., Prumbaum, D., et al. (2019). SPHIRE-crYOLO is a fast and accurate fully automated particle picker for cryo-EM. Commun. Biol. 2, 218.

83. Scheres, S.H.W. (2012). A Bayesian view on cryo-EM structure determination. J. Mol. Biol. *415*, 406–418.

84. Zivanov, J., Nakane, T., Forsberg, B.O., Kimanius, D., Hagen, W.J., Lindahl, E., and Scheres, S.H. (2018). New tools for automated high-resolution cryo-EM structure determination in RELION-3. Elife *7*.

85. Punjani, A., Rubinstein, J.L., Fleet, D.J., and Brubaker, M.A. (2017). cryo-SPARC: algorithms for rapid unsupervised cryo-EM structure determination. Nat. Methods *14*, 290–296.

86. Sanchez-Garcia, R., Gomez-Blanco, J., Cuervo, A., Carazo, J.M., Sorzano, C.O.S., and Vargas, J. (2021). DeepEMhancer: a deep learning solution for cryo-EM volume post-processing. Commun Biol *4*, 874. https://doi.org/10.1038/s42003-021-02399-1.

87. Emsley, P., Lohkamp, B., Scott, W.G., and Cowtan, K. (2010). Features and development of Coot. Acta Crystallogr. D Biol. Crystallogr. *66*, 486–501.

88. Croll, T.I. (2018). ISOLDE: a physically realistic environment for model building into low-resolution electron-density maps. Acta Crystallogr. D Struct. Biol. *74*, 519–530.

89. Adams, P.D., Afonine, P.V., Bunkóczi, G., Chen, V.B., Davis, I.W., Echols, N., Headd, J.J., Hung, L.W., Kapral, G.J., Grosse-Kunstleve, R.W., et al. (2010). PHENIX: a comprehensive Python-based system for macromolecular structure solution. Acta Crystallogr D Biol Crystallogr *66*, 213–221. https://doi.org/10.1107/S0907444909052925.

90. Krissinel, E., and Henrick, K. (2007). Inference of macromolecular assemblies from crystalline state. J. Mol. Biol. *372*, 774–797.

91. Goddard, T.D., Huang, C.C., Meng, E.C., Pettersen, E.F., Couch, G.S., Morris, J.H., and Ferrin, T.E. (2018). UCSF ChimeraX: Meeting modern challenges in visualization and analysis. Protein Sci. *27*, 14–25.

92. Hsieh, C.-L., Goldsmith, J.A., Schaub, J.M., DiVenere, A.M., Kuo, H.-C., Javanmardi, K., Le, K.C., Wrapp, D., Lee, A.G., Liu, Y., et al. (2020). Structure-based design of prefusion-stabilized SARS-CoV-2 spikes. Science *369*, 1501–1505.

93. Meier, S., Güthe, S., Kiefhaber, T., and Grzesiek, S. (2004). Foldon, the natural trimerization domain of T4 fibritin, dissociates into a monomeric A-state form containing a stable beta-hairpin: atomic details of trimer dissociation and local beta-hairpin stability from residual dipolar couplings. J. Mol. Biol. *344*, 1051–1069.

94. ter Meulen, J., van den Brink, E.N., Poon, L.L.M., Marissen, W.E., Leung, C.S.W., Cox, F., Cheung, C.Y., Bakker, A.Q., Bogaards, J.A., van Deventer, E., et al. (2006). Human monoclonal antibody combination against SARS coronavirus: synergy and coverage of escape mutants. PLoS Med. *3*, e237.

95. Case, J.B., Rothlauf, P.W., Chen, R.E., Kafai, N.M., Fox, J.M., Smith, B.K., Shrihari, S., McCune, B.T., Harvey, I.B., Keeler, S.P., et al. (2020). Replication-Competent Vesicular Stomatitis Virus Vaccine Vector Protects against SARS-CoV-2-Mediated Pathogenesis in Mice. Cell Host Microbe *28*, 465–474.e4.

96. Zivanov, J., Nakane, T., and Scheres, S.H.W. (2019). A Bayesian approach to beam-induced motion correction in cryo-EM single-particle analysis. IUCrJ *6*, 5–17.

97. Sanchez-Garcia, R., Gomez-Blanco, J., Cuervo, A., Carazo, J.M., Sorzano, C.O.S., and Vargas, J. (2021). DeepEMhancer: a deep learning solution for Cryo-EM volume post-processing. Commun. Biol. *4*, 874.

98. Mirdita, M., Ovchinnikov, S., and Steinegger, M. (2021). ColabFold - Making Protein Folding Accessible to All.

99. Adams, P.D., Afonine, P.V., Bunkóczi, G., Chen, V.B., Davis, I.W., Echols, N., Headd, J.J., Hung, L.-W., Kapral, G.J., Grosse-Kunstleve, R.W., et al. (2010). PHENIX: a comprehensive Python-based system for macromolecular structure solution. Acta Crystallogr. D Biol. Crystallogr. *66*, 213–221.

STAR★METHODS

KEY RESOURCES TABLE

REAGENT or RESOURCE	SOURCE	IDENTIFIER
Antibodies		
SARS2-57	This paper	N/A
SARS2-35	This paper	N/A
SARS2-50	This paper	N/A
SARS2-56	This paper	N/A
SARS2-47	This paper	N/A
SARS2-40	This paper	N/A
SARS2-29	This paper	N/A
SARS2-69	This paper	N/A
SARS2-11	This paper	N/A
SARS2-12	This paper	N/A
SARS2-30	This paper	N/A
SARS2-68	This paper	N/A
SARS2-36	This paper	N/A
SARS2-24	This paper	N/A
SARS2-51	This paper	N/A
SARS2-28	This paper	N/A
SARS2-13	This paper	N/A
SARS2-20	This paper	N/A
SARS2-17	This paper	N/A
SARS2-26	This paper	N/A
SARS2-64	This paper	N/A
SARS2-38	VanBlargan et al.[32]	N/A
SARS2-02	VanBlargan et al.[32]	N/A
hSARS-57 (chimeric human mAb)	This paper	N/A
hSARS-57 N297Q (human chimeric mAb)	This paper	N/A
COV2-2676	Suryadevara et al.[42]	N/A
CR3022	ter Meulen et al.[78]	N/A
Goat anti-mouse IgG-HRP	Southern Biotech	cat # 1030-05
Anti-Flag-HRP	Sigma	cat # A8592
Bacterial and virus strains		
VSV-SARS-CoV-2 (D614G, BA.1, and escape mutants)	Liu et al.[66] and this paper	N/A
SARS-CoV-2 WA1/2020	Hassan et al.[21]	N/A
SARS-CoV-2 D614G	Chen et al.[49]	N/A
SARS-CoV-2 Wash-B.1.351	Chen et al.[49]	N/A
SARS-CoV-2 Wash-B.1.1.28	Chen et al.[49]	N/A
SARS-CoV-2 B.1.1.7	Chen et al.[49]	N/A
SARS-CoV-2 B.1.429	C. Chiu and R. Andino labs (UCSF)	N/A
SARS-CoV-2 B.1.1.298	BEI Resources	NR-53953
SARS-CoV-2 B.1.617.1	M. Suthar laboratory (Emory University)	N/A
SARS-CoV-2 B.1.617.2	R. Webby laboratory (St. Jude Children's Research Hospital)	N/A

Continued

REAGENT or RESOURCE	SOURCE	IDENTIFIER
SARS-CoV-2 B.1.526	M. Suthar laboratory (Emory University)	N/A
SARS-CoV-2 B.1.630	Peter Halfmann (University of Wisconsin, Madison)	N/A
SARS-CoV-2 B.1.621	Peter Halfmann (University of Wisconsin, Madison)	N/A
SARS-CoV-2 BA.1	Case et al.[61]	N/A
SARS-CoV-2 BA.1.1	Case et al.[61]	N/A
SARS-CoV-2 BA.2	Case et al.[61]	N/A
Chemicals, peptides, and recombinant proteins		
SARS-CoV-2 spike protein	Fremont laboratory	N/A
SARS-CoV-2 spike NTD	P. McTamney, K. Ren, A. Barnes (Astra Zeneca)	N/A
Deposited data		
SARS2-57 structure (local)	This paper	PDB: 7SWW
SARS2-57/NTD EM density map (local)	This paper	EMDB: EMD-25487
SARS2-57/spike structure	This paper	PDB: 7SWX
SARS2-57/spike EM density map	This paper	EMDB: EMD-25488
SARS2-57 VH sequence	This paper	GenBank: MZ703125
SARS2-57 VL sequence	This paper	GenBank: MZ703126
Experimental models: Cell lines		
Vero-E6	ATCC	CRL-1586; RRID: CVCL_0574
Vero+TMPRSS2	Chen et al.[49]	N/A
Vero+TMPRSS2+ACE2	Chen et al.[49]	N/A
Experimental models: Organisms/strains		
K18-hACE2 transgenic mice	Jackson laboratory	strain # 34860
Oligonucleotides		
SARS-CoV-2 qPCR primer 5′-ATGCTGCAATCGTGCTACAA-3′	Case et al.[79]	N/A
SARS-CoV-2 qPCR primer 5′-GACTGCCGCCTCTGCTC-3′	Case et al.[79]	N/A
SARS-CoV-2 qPCR probe 5′-/56-FAM/TCAAGGAAC/Zen/AACATTGCCAA/3IABkFQ-3′	Case et al.[79]	N/A
GAPDH qPCR primer+probe	IDT PrimeTime Assay	Hs.PT.39a.22214836
Software and algorithms		
MotionCor2 v1.3.1	Zheng et al.[80]	N/A
GCTF v1.18	Zhang[81]	N/A
CrYOLO v1.7.6	Wagner et al.[82]	N/A
Relion 3.1	Scheres[83]; Zivanov et al.[84]	N/A
cryoSPARC v3.1.0	Punjani et al.[85]	N/A
DeepEMhancer	Sancez-Garcia et al.[86]	N/A
Coot v0.9.5	Emsley et al.[87]	N/A
Isolde v1.1.0	Croll[88]	N/A
Phenix v1.19	Adams et al.[89]	N/A
qtPISA	Krissinel and Henrick[90]	N/A
UCSF ChimeraX	Goddard et al.[91]	N/A

RESOURCE AVAILABILITY

Lead contact
Further information and requests for resources and reagents should be directed to the lead contact, Daved H. Fremont (fremont@wustl.edu).

Materials availability
All requests for resources or reagents should be directed to the lead contact. This includes viruses, proteins, and cells. Reagents will be made available upon request after completion of a Materials Transfer Agreement.

Data and code availability
All data supporting the findings of this study are available within the paper and from the corresponding author upon request. This paper does not include original code. All structures have been deposited in the PDB and EMDB databases (PDB: 7SWW and 7SWX; EMDB: 25487 and 25488). Any additional information required to reanalyze the data reported in this work paper is available from the lead contactupon request.

EXPERIMENTAL MODEL AND PARTICIPANT DETAILS

Cells
Cell lines were maintained at 37°C in the presence of 5% CO_2. Vero E6 cells were passaged in Dulbecco's modified Eagle Medium (DMEM) (Invitrogen) supplemented with 10% fetal bovine serum (FBS) (Omega Scientific) and 100 U/mL penicillin-streptomycin (P/S) (Invitrogen). Vero cells that over-express TMPRSS2 or TMPRSS2-ACE2 were maintained as Vero CCL81 cells, with the addition of 5 μg/mL blasticidin (Vero-TMPRSS2) or 10 μg/mL puromycin (Vero-TMPRSS2-ACE2).

Viruses
The 2019n-CoV/USA_WA1/2020 (WA1/2020) isolate of SARS-CoV-2 was obtained from the US Centers for Disease Control (CDC). WA1/2020 stocks were propagated on Vero CCL81 cells and used at passage 6 and 7. For experiments with a sequence-confirmed intact furin cleavage site, WA1/2020 was passaged twice on Vero+TMPRSS2 cells. The D614G virus was produced by introducing the mutation into an infectious clone of WA1/2020, and the B.1.351 and B.1.1.28 spike genes were cloned into the WA1/2020 infectious clone to produce Wash-B.1.351 and Wash-B.1.1.28 chimeric viruses, as described previously.[9,49] The B.1.1.7, B.1.429, B.1.1.298, B.1.617.1, B.1.617.2, B.1.526, B.1.630, B.1.621, BA.1, BA.1.1, and BA.2 viruses were isolated from infected individuals. Viruses were propagated on Vero-TMPRSS2 cells and subjected to deep sequencing to confirm the presence of the substitutions indicated in Figure 6C. Viral titer was determined by focus-forming assay (FFA) on Vero+TMPRSS2+ACE2 cells as described.[79]

Mouse studies
Animal studies were carried out in accordance with the recommendations in the Guide for the Care and Use of Laboratory Animals of the National Institutes of Health. The protocols were approved by the Institutional Animal Care and Use Committee at the Washington University School of Medicine (Assurance number A3381-01). Virus inoculations were performed under anesthesia that was induced and maintained with ketamine hydrochloride and xylazine, and all efforts were made to minimize animal suffering.

K18-hACE2 transgenic mice were purchased from Jackson Laboratories (#034860) and housed in a pathogen-free animal facility at Washington University in St. Louis. For passive transfer studies, mAbs were diluted in PBS and administered to mice via intraperitoneal injection in a 100 μL total volume. Viral infections were performed via intranasal inoculation with 10^3 FFU. Mice were monitored daily for weight loss.

METHOD DETAILS

Proteins
The gene encoding SARS-CoV-2 S protein (residues 1–1213, GenBank: MN908947.3) was cloned into a pCAGGS mammalian expression vector with a C-terminal hexahistidine tag. The S protein was prefusion stabilized and expression optimized via six proline substitutions (F817P, A892P, A899P, A942P, K986P, V987P)[92] with a disrupted S1/S2 furin cleavage site and a C-terminal foldon trimerization motif.[93] Expi293F cells were transiently transfected, and proteins were recovered via cobalt-charged resin chromatography (G-Biosciences) as previously described.[13] For ACE2 binding inhibition analysis, the SARS-CoV-2 S protein was made by synthesizing a gene encoding the ectodomain of a prefusion conformation-stabilized SARS-CoV-2 spike (S6P$_{ecto}$) protein[92] containing C-terminal Twin-Strep-tag. The S gene was then cloned it into a DNA plasmid expression vector for mammalian cells. Protein was produced in FreeStyle 293-F cells (Thermo Fisher Scientific) and purified from culture supernatants using StrepTrap HP affinity column (Cytiva).

MAb generation

BALB/c mice were immunized with 10 μg of SARS-CoV-2 RBD adjuvanted with 50% AddaVax (InvivoGen), via intramuscular route (i.m.), followed by i.m. immunization two and four weeks later with SARS-CoV-2 spike protein (5 μg and 10 μg, respectively) supplemented with AddaVax. Mice received a final, non-adjuvanted boost of 25 μg of SARS-CoV-2 spike or RBD (12.5 μg intravenously and 12.5 μg interperitoneally) 3 days prior to fusion of splenocytes with P3X63.Ag.6.5.3 myeloma cells. Hybridomas producing antibodies that bound to SARS-CoV-2-infected permeabilized Vero CCL81 cells by flow cytometry and to SARS-CoV-2 recombinant S protein by direct ELISA were cloned by limiting dilution. A subset of neutralizing hybridoma supernatants were purified commercially (Bio X Cell) after adaptation for growth under serum-free conditions.

NTD-binding ELISA

Wells of 96-well microtiter plates were coated with purified recombinant SARS-CoV-2 S-NTD (kindly provided by P. McTamney, K. Ren and A. Barnes, Astra Zeneca) at 4°C overnight. Plates were blocked with 2% non-fat dry milk and 2% normal goat serum in DPBS containing 0.05% Tween 20 (DPBS-T) for 1 h. For screening assays, hybridoma culture supernatants were diluted 1:5 in blocking buffer, added to the wells in duplicate, and incubated for 1 h at ambient temperature. The bound antibodies were detected using goat anti-mouse IgG antibody conjugated with horseradish peroxidase (Southern Biotech, cat# 1030-05, 1:5,000 dilution for the assay) and TMB substrate (Thermo Fisher Scientific). Color development was monitored, 1 N Hydrochloric acid was added to stop the reaction and the absorbance was measured at 450 nm using a spectrophotometer (Biotek).

Competition-binding analysis

The assay was performed as described previously.[35] Briefly, for screening study wells of 384-well microtiter plates were coated with 1 μg/mL of purified SARS-CoV-2 S6P$_{ecto}$ protein at 4°C overnight. Plates were blocked with 2% bovine serum albumin (BSA) in DPBS-T for 1 h. Murine hybridoma culture supernatants were diluted 5-fold in blocking buffer, added to the wells (20 μL per well) in duplicates for each tested reference mAb and incubated for 1 h at ambient temperature. Biotinylated reference human mAbs of known binding specificity [COV2-2676[42] and CR3022[94]] were added to each of well with the respective hybridoma culture supernatant at 1.25 μg/mL in a volume of 5 μL per well (final concentration of biotinylated monoclonal antibody 0.25 μg/mL) without washing of the plates, and then incubated for 1 h at ambient temperature. Plates were washed, and bound antibodies were detected using HRP-conjugated avidin (Sigma, cat# A3151, 0.3 μg/mL final concentration) and a TMB substrate. The signal obtained for binding of the biotin-labeled reference antibody in the presence of the hybridoma culture supernatant was expressed as a percentage of the binding of the reference antibody alone after subtracting the background signal. Tested mAbs were considered competing if their presence reduced the reference antibody binding to less than 41% of its maximal binding and non-competing if the signal was greater than 71%. A level of 40–70% was considered intermediate competition.

Human ACE2 binding inhibition analysis

The assay was performed as described previously.[35] Briefly, for screening study wells of 384-well microtiter plates were coated with 1 μg/mL purified recombinant SARS-CoV-2 S6P$_{ecto}$ protein at 4°C overnight. Plates were blocked with 2% non-fat dry milk and 2% normal goat serum in DPBS-T for 1 h. Mouse hybridoma culture supernatants were diluted 5-fold in blocking buffer, added to the wells (20 μL per well) in quadruplicate, and incubated for 1 h at ambient temperature. Recombinant human ACE2 with a C-terminal FLAG tag peptide was added to wells at 2 μg/mL in a 5 μL per well volume (final 0.4 μg/mL concentration of human ACE2) without washing of the plates, and then incubated for 40 min at ambient temperature. Plates were washed, and bound human ACE2 was detected using HRP-conjugated anti-Flag antibody (Sigma-Aldrich, cat. A8592, lot SLBV3799, 1:5,000 dilution) and TMB substrate. ACE2 binding without antibody served as a control for maximal binding. Antibody COV2-2196 (RBD) served as a control for ACE2 binding inhibition. The signal obtained for binding of the human ACE2 in the presence of each dilution of tested culture supernatant was expressed as a percentage of the human ACE2 binding without antibody after subtracting the background signal.

VSV-eGFP-SARS-CoV-2-S escape mutants

VSV-eGFP-SARS-CoV-2-S escape mutants were produced as described previously.[66] Briefly, plaque assays were performed to isolate escape mutants on Vero cells with neutralizing mAb in the overlay. Resistant clones were plaque-purified on Vero-TMPRSS2 cells in the presence of mAb. Plaques in agarose plugs and viral stocks were amplified on MA104 cells at an MOI of 0.01 in Medium 199 containing 2% FBS and 20 mM HEPES pH 7.7 (Millipore Sigma) at 34°C. Viral supernatants were harvested upon extensive cytopathic effect and clarified of cell debris by centrifugation at 1,000 x g for 5 min. Aliquots were maintained at −80°C. Viral RNA was extracted from VSV-SARS-CoV-2 mutant viruses using RNeasy Mini kit (Qiagen), and S was amplified using OneStep RT-PCR Kit (Qiagen). The mutations were identified by Sanger sequencing (GENEWIZ). Their resistance was verified by subsequent virus infection in the presence or absence of antibody. Briefly, Vero cells were seeded into 12 well plates for approximately 12 h. Virus was serially diluted using DMEM and cells were inoculated at 37°C for 1 h. Cells were cultured with an agarose overlay in the presence or absence of mAb at 34°C for 2 days. Plates were scanned on a biomolecular imager and expression of eGFP is shown at 48 h post-infection.

Determination of mAb concentration in hybridoma supernatant

The mAb concentration in hybridoma supernatant was quantified by ELISA. Nunc MaxiSorp plates (Thermo Fisher Scientific) were coated with 1 μg/mL of goat anti-mouse IgG (Southern Biotech) in 50 μL of NaHCO$_3$ (pH 9.6) coating buffer and incubated overnight at 4°C. Plates were washed three times with ELISA wash buffer (PBS containing 0.05% Tween 20), and then incubated with 200 μL of blocking buffer (PBS, 2% BSA, 0.05% Tween 20) for 1 h at room temperature. Plates were incubated with hybridoma supernatant diluted 1:500 or 1:2,000 in blocking buffer, or serial dilutions of purified isotype control mAb as a standard, for 1 h at room temperature. Plates were washed three times with ELISA wash buffer and incubated with 50 μL of anti-mouse IgG-HRP (Sigma) diluted 1:500 for 1 h at room temperature. Plates were washed three times with ELISA wash buffer and three times with PBS, before incubation with 100 μL of TMB substrate (Thermo Fisher Scientific) for 3 min at room temperature before quenching with the addition of 50 μL of 2 N H$_2$SO$_4$ and measuring OD 450 nm. Antibody concentrations in hybridoma supernatant were interpolated from a standard curve produced using an isotype control mAb.

Neutralization assay

FRNTs were performed as described previously.[79] Briefly, serial dilutions of antibody were incubated with 2 x 10^2 FFU of SARS-CoV-2 for 1 h at 37°C. Immune complexes were added to cell monolayers (Vero E6 cells or other cell lines where indicated) and incubated for 1 h at 37°C prior to the addition of 1% (w/v) methylcellulose in MEM. Following incubation for 30 h at 37°C, cells were fixed with 4% paraformaldehyde (PFA), permeabilized and stained for infection foci with SARS2-16 (hybridoma supernatant diluted 1:6,000 to a final concentration of ∼20 ng/mL). Antibody-dose response curves were analyzed using non-linear regression analysis (with a variable slope) (GraphPad Software). The antibody concentration required to reduce infection by half (EC$_{50}$) was determined.

Pre- and post-attachment neutralization assays

For pre-attachment assays, serial dilutions of mAbs were prepared at 4°C in Dulbecco's modified Eagle medium (DMEM) with 2% FBS and preincubated with 10^2 FFU of SARS-CoV-2 for 1 h at 4°C. MAb-virus complexes were added to a monolayer of Vero cells for 1 h at 4°C. Virus was allowed to internalize during a 37°C incubation for 30 min. Cells were overlaid with 1% (w/v) methylcellulose in MEM. For post-attachment assays, 2 x 10^2 FFU of SARS-CoV-2 was adsorbed onto a monolayer of Vero cells for 1 h at 4°C. After removal of unbound virus, cells were washed twice with cold DMEM, followed by the addition of serial dilutions of MAbs in cold DMEM. Virus-adsorbed cells were incubated with mAb dilutions for 1 h at 4°C. Virus then was allowed to internalize for 30 min at 37°C, and subsequently cells were overlaid with methylcellulose as described above. Thirty hours later, plates were fixed with 4% PFA and analyzed for antigen-specific foci as described above for FRNTs.

Attachment inhibition assay

SARS-CoV-2 was incubated with mAbs at 10 μg/mL for 1 h at 4°C. The mixture was added to pre-chilled Vero E6, Vero-TMPRSS2, or Vero-TMPRSS2-ACE2 at an MOI of 0.005 and incubated at 4°C for 1 h. Cells were washed six times with chilled PBS before addition of lysis buffer and extraction of RNA using MagMax viral RNA isolation kit (Thermo Fisher Scientific) and a Kingfisher Flex 96-well extraction machine (Thermo Fisher Scientific). SARS-CoV-2 RNA was quantified by qRT-PCR using the *N*-specific primer/probe set described below. *GAPDH* was measured using a predesigned primer/probe set (IDT PrimeTime Assay Hs.PT.39a.22214836). Viral RNA levels were normalized to GAPDH, and the fold change was compared with isotype control mAb. For each cell type, a control with a 4-fold lower MOI (0.00125) was included to demonstrate detection of decreased viral RNA levels.

Virus internalization assay

SARS-CoV-2 was incubated with mAbs at 10 μg/mL for 1 h at 4°C. The mixture was added to pre-chilled Vero E6 cells at an MOI of 0.005 and incubated at 4°C for 1 h. Cells were washed twice with chilled PBS to remove unbound virus, and subsequently incubated in DMEM at 37°C for 30 min to allow virus internalization. Cells then were treated with proteinase K and RNaseA at 37°C for 10 min to removed uninternalized virus. Viral and cellular RNA were extracted and analyzed as described above for the attachment inhibition assay. A no internalization control was included, where proteinase K and RNase A treatments were performed directly after washing, without an internalization step.

Syncytia formation assay

Vero E6-TMPRSS2 cells[95] were seeded into 12-well plates with 1 mL of DMEM and 10% FBS without antibiotics and grown to confluency overnight. Cells were then inoculated with VSV-SARS-CoV-2 S D614G or BA.1 at a multiplicity of infection (MOI) of 3.0. After 1 h, infection media was removed, the cells were washed with 1x Hanks' Balanced Salt Solution (HBSS), then 1 mL of DMEM with or without mAb SARS2-57 (final concentration of 1.4 μg/mL) was added. Cells were imaged 12 h post-infection.

Anti-SARS-CoV-2 mAb binding to the surface of infected cells

Vero E6 cells or Vero-TMPRSS2 cells were inoculated with SARS-CoV-2 at a multiplicity of infection (MOI) of 0.01. At 48 h post-infection, cells were trypsinized and resuspended in a staining buffer composed of PBS with 5% FBS, 5 mM EDTA, 0.05% NaN$_3$. MAbs were diluted in the staining buffer and incubated with ∼3 x 10^4 cells for 30 min at 4°C. Cells were washed twice and incubated with

Alexa Fluor 647-conjugated secondary antibody (Invitrogen) diluted 1:1000 in staining buffer for 30 min at 4°C. Cells were washed twice and fixed with 4% PFA prior to detection of fluorescence signal by flow cytometry (MacsQuant) and analysis using FlowJo software.

Sequencing, cloning, and expression of chimeric IgG1

To generate chimeric human IgG1 from the SARS2-57 mouse hybridoma cell line, cells were lysed in Trizol (Thermo) followed by RNA purification with Direct-Zol Micro kit (Zymo). 5′ RACE products were generated with Template Switching RT Enzyme Mix (New England Biolabs) using anchored poly(dT)23 and TSO (GCT AAT CAT TGC AAG CAG TGG TAT CAA CGC AGA GTA CAT rGrGrG) oligonucleotides according to the manufacturer's instructions. Heavy and light chain sequences were amplified with primers specific for the TSO handle-sequence and the respective constant region sequence with Q5 Polymerase (New England Biolabs). Following Sanger sequencing, full-length variable regions were synthesized as gene blocks (Integrated DNA Technologies) and cloned into hIgG1 (wild-type or N297Q) and hKappa expression vectors by Gibson assembly. Variable regions sequences are available on GenBank (heavy chain accession MZ703125 and light chain accession MZ703126). Recombinant antibodies were expressed in Expi293 cells following co-transfection of heavy and light chain plasmids (1:1 ratio) using Expifectamine 293 (Thermo Fisher Scientific). Supernatants were harvested after 5–6 days, purified by affinity chromatography (Protein A Sepharose, GE), and desalted with a PD-10 (Cytiva) column.

Measurement of viral burden and cytokine and chemokine levels

On 7 dpi, mice were euthanized and organs were collected. Nasal washes were collected in 0.5 mL of PBS. Organs were weighed and homogenized using a MagNA Lyser (Roche). Viral RNA from homogenized organs or nasal wash was isolated using the MagMAX Viral RNA Isolation Kit (ThermoFisher) and measured by TaqMan one-step quantitative reverse-transcription PCR (RT-qPCR) on an ABI 7500 Fast Instrument. Viral burden is expressed on a log_{10} scale as viral RNA (N gene) per mg for each organ or total nasal wash after comparison with a standard curve produced using serial 10-fold dilutions of viral RNA standard. Primers were 5′-ATGCTGCAATCGTGCTACAA-3′, 5′- GACTGCCGCCTCTGCTC-3′, and probe 5′-/56-FAM/TCAAGGAAC/Zen/AACATTGCCAA/3IABkFQ-3′ (Case et al., 2020). For the measurement of cytokine and chemokine levels in the lung, tissue homogenates were treated with 1% Triton X-100 for 1 h at room temperature to inactivate virus. Cytokine and chemokine levels in the lung homogenate were then analyzed by multiplex array (Eve Technologies Corporation).

Binding analysis via biolayer interferometry

Biolayer interferometry (BLI) was used to quantify the binding capacity of SARS2-57 Fab fragments to trimerized SARS-CoV-2 S protein. 10 μg/mL of biotinylated S was immobilized onto streptavidin biosensors (ForteBio) for 4 min. After a 30 s wash, the pins were submerged in running buffer (10 mM HEPES, 150 mM NaCl, 3 mM EDTA, 0.05% P20 surfactant, and 1% BSA) containing SARS2-57 Fab ranging from 0.4 to 409.6 nM, followed by a dissociation step in running buffer alone. The BLI signal was recorded and globally fit to a 1:1 binding model using ForteBio Data Analysis software (v9.0). Binding was evaluated in triplicate.

Cryo-EM sample preparation

Data were collected on lacey carbon grids with or without ultra-thin carbon film. For standard lacey carbon grids (Ted Pella #01895-F), SARS-CoV-2 S protein was prepared at 1 mg/mL in TBS (30 mM Tris pH 8, 150 mM NaCl). For lacey carbon grids with ultra-thin carbon film (Ted Pella #01824G), SARS-CoV-2 S protein was prepared at 0.2 mg/mL in TBS. Each sample was incubated for 15 min with 1 M equivalent of SARS2-57 Fab fragments, applied to glow-discharged grids, then flash-frozen in liquid ethane using a Vitrobot Mark IV (ThermoFisher Scientific).

Cryo-EM data collection

Grids were loaded into a Cs-corrected FEI Titan Krios 300kV microscope equipped with a Gatan K2 direct electron detector and a BioQuantum 968 energy filter operating in zero loss mode with a 20eV slit. Images were collected at a nominal magnification of 105,000×, resulting in a calibrated pixel size of 1.1 Å. Each movie consisted of 45 frames at 200 ms each with a dose of 1.49 e−/Å²/frame, yielding a total dose of 66.9e-/Å²/movie.

Cryo-EM data processing

Movies were motion corrected using MotionCor2 v1.3.1,[80] and contrast transfer function parameters were estimated using GCTF v1.18.[81] Particles were picked in CrYOLO v1.7.6[82] using a general model for standard lacey carbon grids and a trained model for lacey carbon grids with ultra-thin film. After one round of 2D classification in Relion 3.1,[83,84] particles from either grid type with clear spike density were merged then aligned to a low-pass filtered spike reference with C3 symmetry imposed.

To identify NTDs bound by Fab, these aligned particles were C3 symmetry expanded then subjected to focused classification of one NTD/Fv using a wide mask (K = 8, T = 16, no image alignment), and classes with clear Fv density were selected. These particles were then refined in C1 with local angular searches only, and a second round of focused classification was performed using a tighter NTD/Fv mask (K = 5, T = 16, no image alignment). The class of highest resolution was then subjected to Bayesian polishing and per-particle CTF refinement in Relion 3.1,[96] followed by non-uniform refinement with local angular searches in cryoSPARC v3.1.0,[85]

generating a map of trimeric spike bound by a single Fab. Finally, to improve resolution at the binding interface, we performed local nonuniform refinement of the NTD/Fv. Final maps were sharpened via deep learning employed through DeepEMhancer.[97]

Model building

The focused map was used to construct a model of the NTD bound by SARS2-57 Fv. An initial model for the NTD was adapted from a cryo-EM structure of spike with complete NTD loops (PDB 7A97). Initial modeling of the SARS2-57 Fv was performed using AlphaFold2, as implemented in ColabFold,[98] with the VH and VL input as a continuous sequence with a polyglycine linker. These starting components were combined and docked into the map, then refined in Coot v0.9.5,[87] Isolde v1.1.0,[88] and Phenix v1.19.[99] Epitope and paratope contacts were identified using Proteins, Interfaces, Structures, and Assemblies (PISA) solvent exclusion analysis,[90] and structures were visualized using UCSF ChimeraX.[91]

The full S trimer map was used to construct a model of S bound by one Fv with all RBDs in the down position. An initial model was generated by combining the locally refined Fv/NTD structure with a previously solved cryo-EM structure of trimeric SARS-CoV-2 S in the proper RBD configuration (PDB 7DWY). This model was docked into the full-spike map then refined using Coot v0.9.5, Isolde v1.1.0, and Phenix v1.19.

Hydrogen-deuterium exchange (HDX) mass spectrometry peptide mapping

To prepare for acquisition and analysis of HDX data, peptide maps (in triplicate) of SARS-CoV-2 spike protein were generated by LC/MS/MS using a Thermo LTQ Orbitrap XL mass spectrometer (Waltham, MA) and a Maxis-II-HM mass spectrometer (Bruker Daltonics, Billerica, MA). SARS-CoV-2 S protein (100 pmol) was injected into the LC-MS system where the protein was digested by passing it through two protease columns in tandem (immobilized pepsin followed by immobilized acid protease from fungal-XIII). Resulting peptides were captured and desalted on a C-8 trap column followed by loading onto a C-18 column and eluting into the mass spectrometer. The instrument was operated in a data-dependent fragmentation mode to monitor the most abundant peptides. Data were analyzed with ByonicTM (Protein Metrics, Santa Carlos, CA, USA) for sequencing and determining the accurate precursor mass (± 5 ppm); the resulting peptides were manually curated. To reduce the protein and denature it, a quench solution containing the reducing agent (tris-(2-carboxyethyl) phosphine hydrochloride or TCEP, 500 mM) and denaturant (guanidine hydrochloride, GdnHCl, 4 M) was used. The quenching conditions were 1:1 dilution of HDX reaction volume (100 μL) with quench buffer to give a pH 2.6 final, 3 min incubation, 25°C.

Epitope mapping by HDX

SARS-CoV-2 spike (100 pmol, 20 μL) was equilibrated without or with antibody (1:2 antibody) in HBS (HEPES buffered saline, pH 7.4) at 25°C for 30 min then diluted 5-fold with D_2O in HBS at 25°C (80 μL). Deuteration extent was measured at 0 (undeuterated control), 10, 60, 300, or 3900 s at 25°C. The HDX was quenched by adding an equal volume of quench buffer at 25°C with mixing for 3 min.

The quenched sample was digested by passing it through a custom-packed column (2 mm × 20 mm) of immobilized pepsin beads followed by a column of immobilized Fungal XIII beads (2 mm × 20 mm) at 200 μL/min flow rate. The resulting peptides were captured and desalted on a Zorbax Eclipse XDB-C8 trap (Agilent) column by using 0.1% formic acid in water for 4.7 min. Desalted peptides were loaded on a C-18 analytical column (2.1 × 50 mm in size, 2.5 μm Xselect-CSH from Waters, Milford, MA) where peptides were separated by using a gradient of acetonitrile (ACN) in 0.1% formic acid (most peptides eluted during the linear part of gradient from 5 min (4% ACN) to 15 min (40% ACN)). To minimize back exchange, the trap and analytical columns were kept in an ice slush. The isotope distributions of the exchanged peptides were measured with a Thermo LTQ Orbitrap XL mass spectrometer (MS only mode) for duplicate samples.

HDX data analysis

LC-MS HDX data acquisition was directed by retention time, isotopic distribution and observed m/z from the peptide map, and data were analyzed by HDExaminer (Sierra Analytics). The maximum deuterium level was set to 80%, and the data displayed as kinetic plots for each peptide. Only those peptides that provided good signal-to-noise ratio at all the time points and for both the states were included, providing a mixture of 338 unique peptides covering ~85% sequence of SARS-CoV-2 spike protein (Figure S2A). The average peptide length was 13 amino acids, and the average residue level redundancy was 3. To elucidate those regions where HDX changed upon antibody binding, a mean cumulative difference (bound - unbound) across all the time points for each peptide was calculated and displayed as a Woods plot. To identify significant differences upon binding, the propagated errors for the cumulative percent deuteration difference for each peptide were calculated using standard error of mean, and 99% confidence was determined (2 degrees of freedom, two tail distribution).

### QUANTIFICATION AND STATISTICAL ANALYSES

Statistical significance was assigned when p values were <0.05 using Prism version 8 (GraphPad). Tests, number of animals (n), median values, and statistical comparison groups are indicated in the Figure legends.

Supplemental information

A broadly reactive antibody targeting

# the N-terminal domain of SARS-CoV-2

spike confers Fc-mediated protection

Lucas J. Adams, Laura A. VanBlargan, Zhuoming Liu, Pavlo Gilchuk, Haiyan Zhao, Rita E. Chen, Saravanan Raju, Zhenlu Chong, Bradley M. Whitener, Swathi Shrihari, Prashant N. Jethva, Michael L. Gross, James E. Crowe Jr., Sean P.J. Whelan, Michael S. Diamond, and Daved H. Fremont
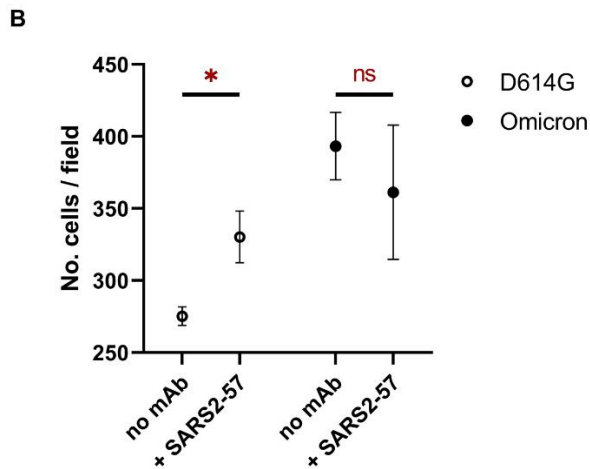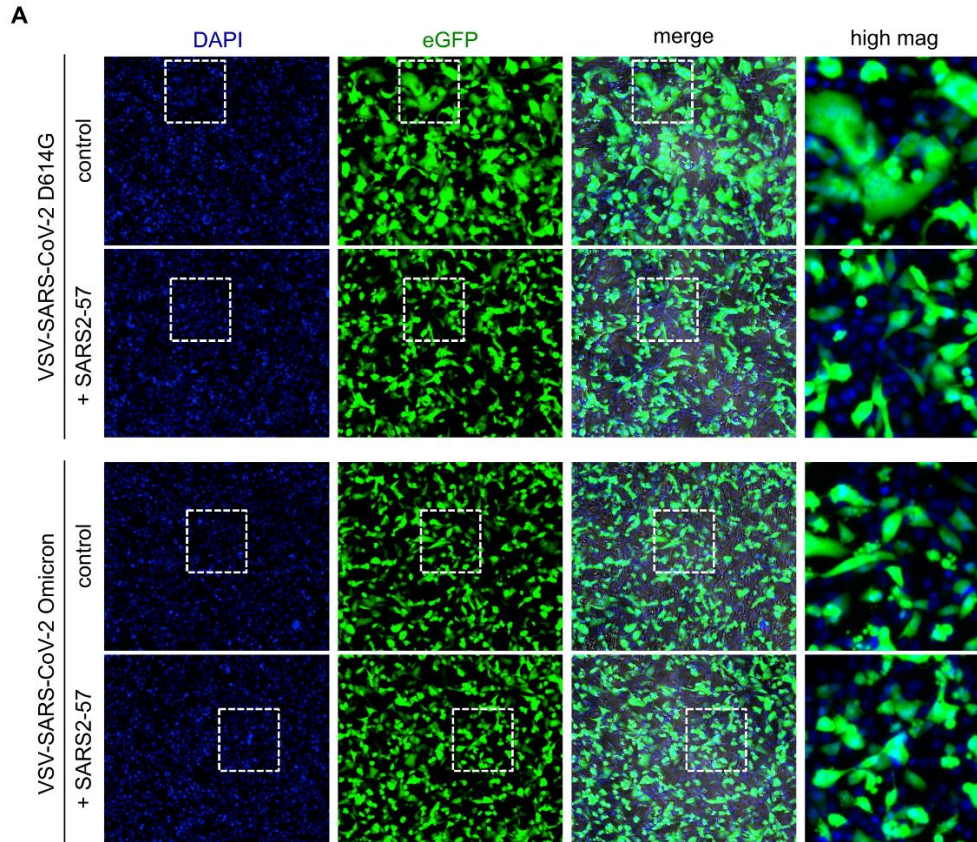
Figure S1. Syncytia formation of VSV-SARS-CoV-2 infected cells inhibited by treatment with mAb SARS2-57. Related to Figure 2. Cell-cell fusion was evaluated using fluorescence microscopy. **(A)** Representative images of cells infected with VSV-SARS-CoV-2 chimeric viruses expressing WT (D614G) or BA.1 S protein, with or without SARS2-57 treatment. **(B)** Number of fluorescent bodies per field is plotted. Randomly selected images (n = 3 per group) were manually evaluated by a blinded experimenter. Student's t-test comparing control and treatment groups: ns, not significant, *p < 0.05.
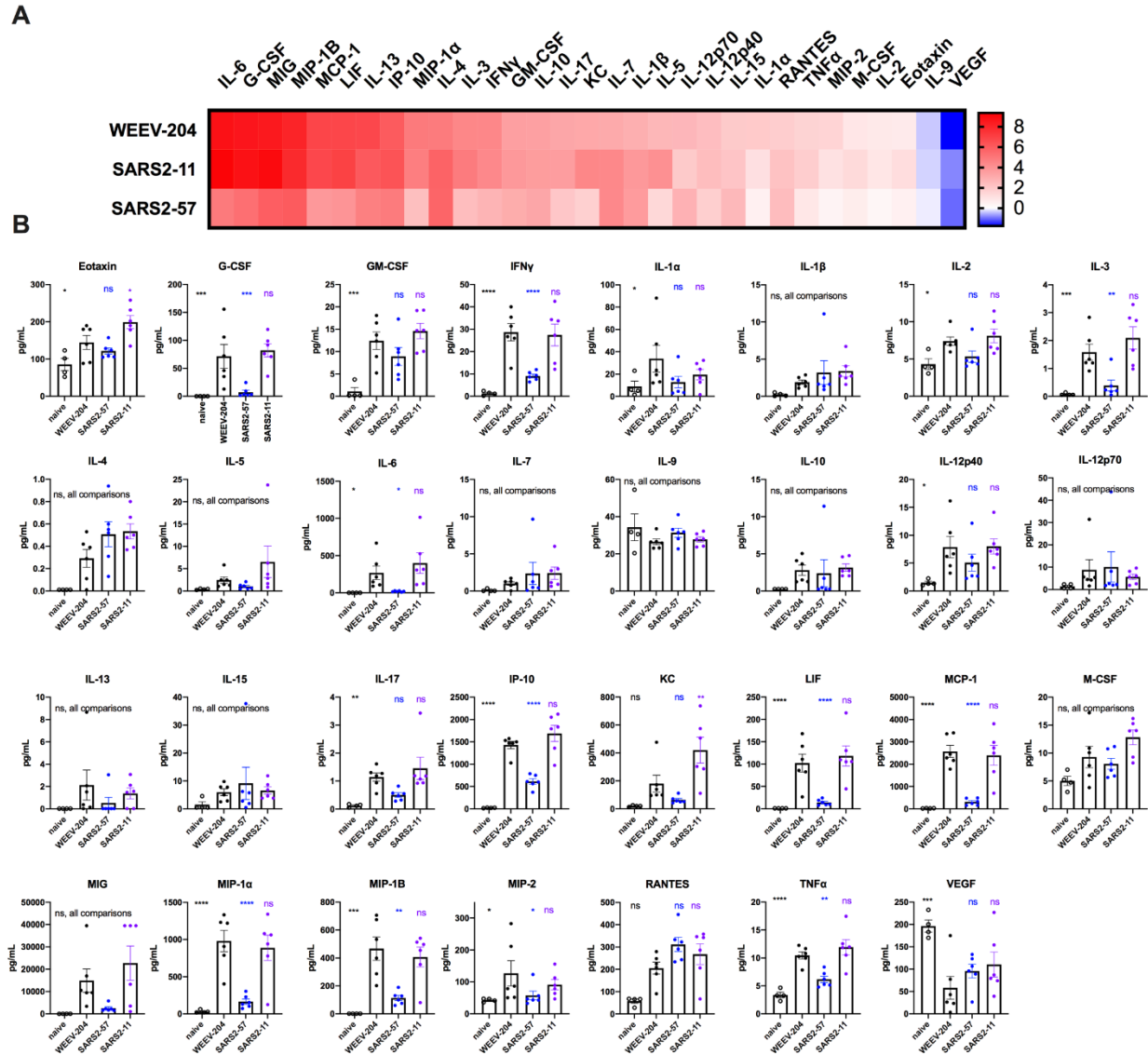
Figure S2. Cytokine and chemokine levels in the lungs of SARS-CoV-2 infected mice following treatment with anti-SARS-CoV2 mAbs. Related to Figure 4. Cytokine and chemokine levels in lung homogenates harvested in Figure 4 were measured by a multiplex platform. **(A)** Heat map showing log2 fold change in cytokine and chemokine levels compared to lungs from mock-infected animals. **(B)** Levels of each cytokine and chemokine are plotted. Data are from two experiments, n = 5-6 per group. One-way ANOVA with Dunnett's post hoc test comparing each result to WEEV-204 isotype control: ns, not significant, ∗p < 0.05, ∗∗p < 0.01, ∗∗∗p < 0.001, ∗∗∗∗p < 0.0001.
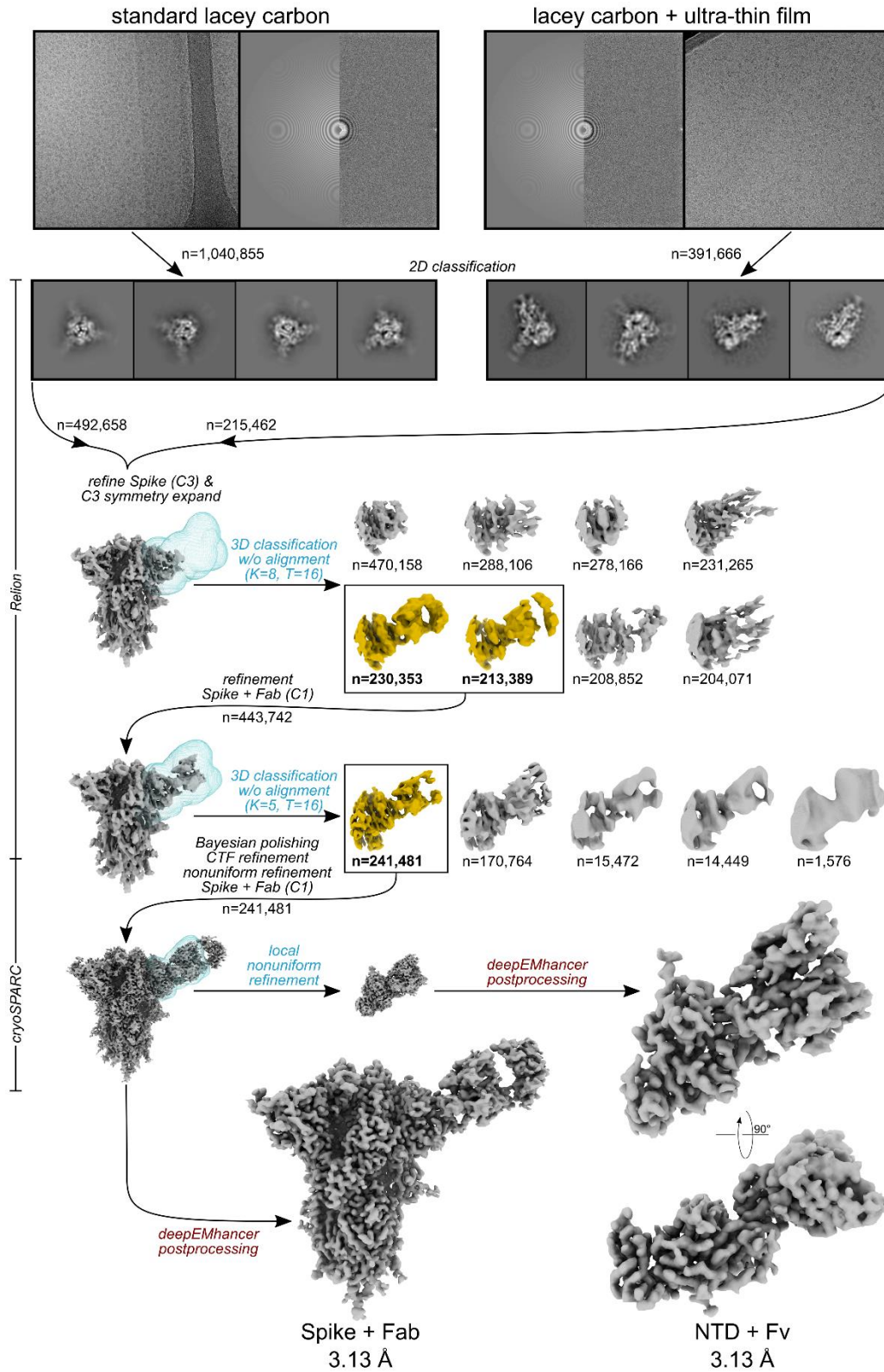
Figure S3. Cryo-EM data processing pipeline. Related to Figure 5. Flowchart depicting data processing steps for global reconstruction of SARS2-57 Fab bound to trimeric S and focused reconstruction of SARS2-57 Fv bound to NTD.
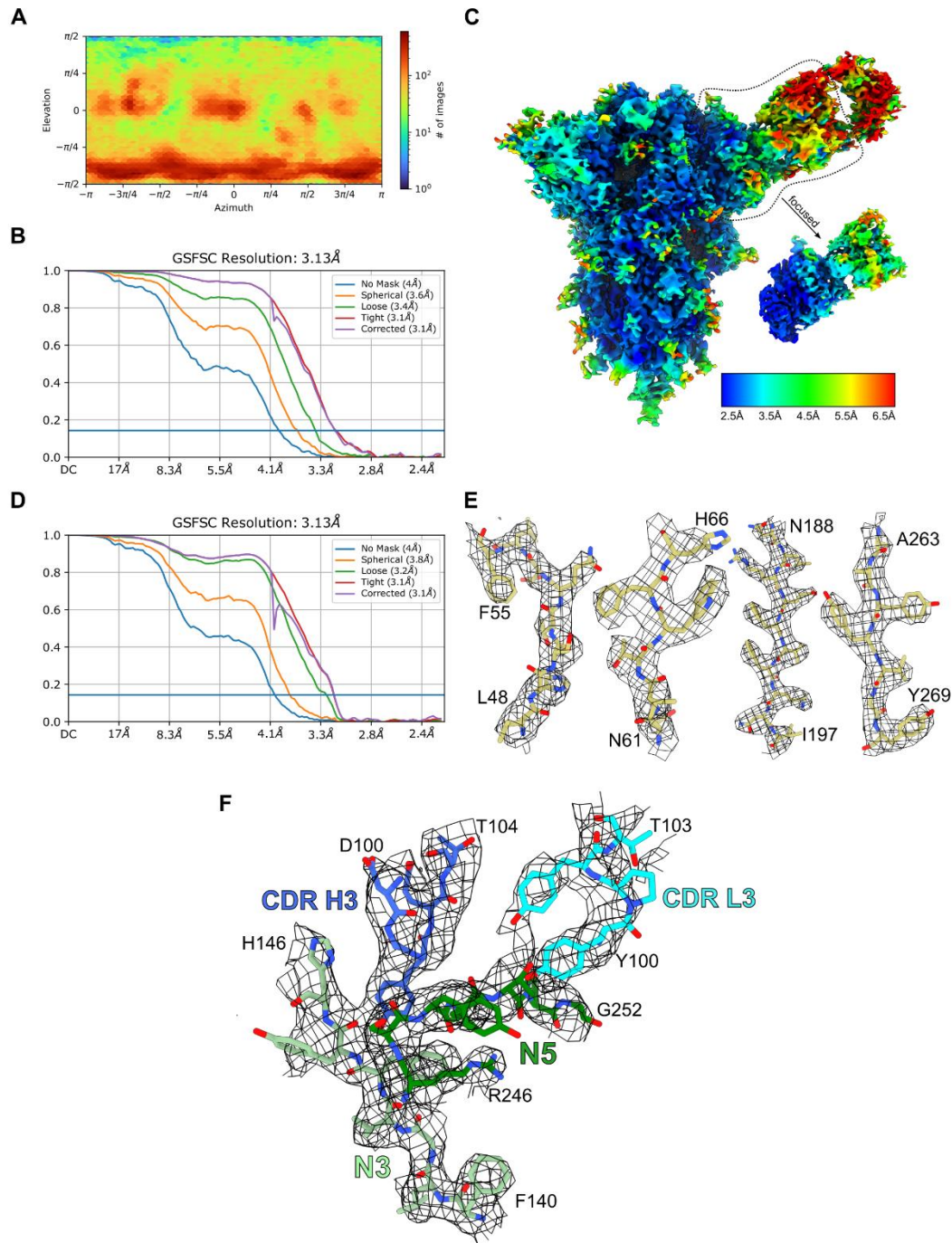
Figure S4. Validation of global and focused cryo-EM reconstructions of SARS2-57 Fab bound to SARS-CoV-2 spike/NTD. Related to Figure 5. (A) Orientational distribution assigned to particles in global refinement of SARS2-57 Fab bound to trimeric S protein. **(B)** GSFSC curve for global refinement of SARS2-57 Fab bound to trimeric S protein. **(C)** Local resolution map for global refinement of SARS2-57 Fab bound to trimeric S protein. **(D)** GSFSC curve for focused refinement of SARS2-57 Fv bound to NTD. **(E)** Example density and model fits for NTD beta strands in focused reconstruction. **(F)** Example density and model fit for SARS2-57/NTD interface. NTD loops N3 or N5 are depicted in mint or forest green, respectively, and SARS2-57 heavy and light chains are depicted in royal blue and cyan, respectively.
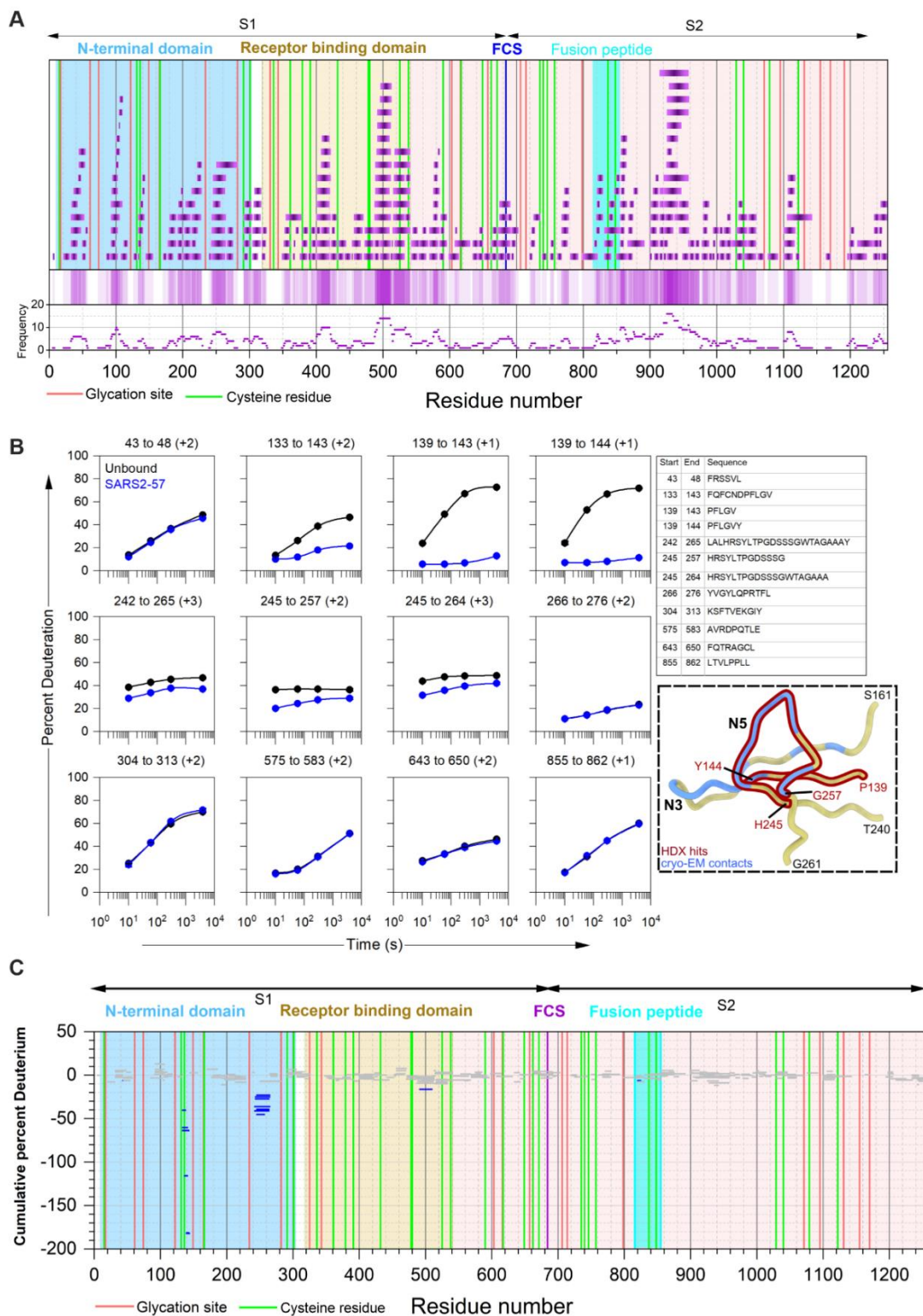
Figure S5. Epitope mapping for SARS2-57 antibody by differential HDX-MS. Related to Figures 5 and 6. (A) Peptide map for the peptides analyzed for differential HDX-MS. Middle graph shows peptides

in overlapping configuration. Violet shading intensity indicates a greater number of peptides covering that region. Bottom graph shows the redundancy for each peptide (i.e., the number of peptides (frequency) covering a given amino acid). In total 338 unique peptides, covering ~85% sequence S protein (redundancy frequency of 3 and average peptide length 13), were analyzed for epitope mapping. **(B)** Representative kinetic plots for the twelve different peptides showing effects of antibody binding on HDX. Black and blue lines are for SARS-CoV-2 S protein in the absence of antibody and in the presence of SARS2-57 antibody, respectively. At the top of each panel are the residue numbers and charge states of the peptide. Sequences of each peptide are in the table. Error bars represent standard error of mean from duplicate measurements. A structural inset compares highly protected residues from HDX (outlined in red) with contact residues as defined by cryo-EM (blue). **(C)** Woods plots showing accumulated difference in % deuteration (bound state - unbound state) across all time points for each analyzed peptide. Propagated error for cumulative difference was calculated for each respective peptide, and 99% confidence intervals were calculated. Peptides whose differential exchange exceeded the 99% confidence interval were considered significant. Peptides that do not show any change or show differences that were insignificant are indicated in gray, and peptides that become more protected upon binding are indicated in blue.
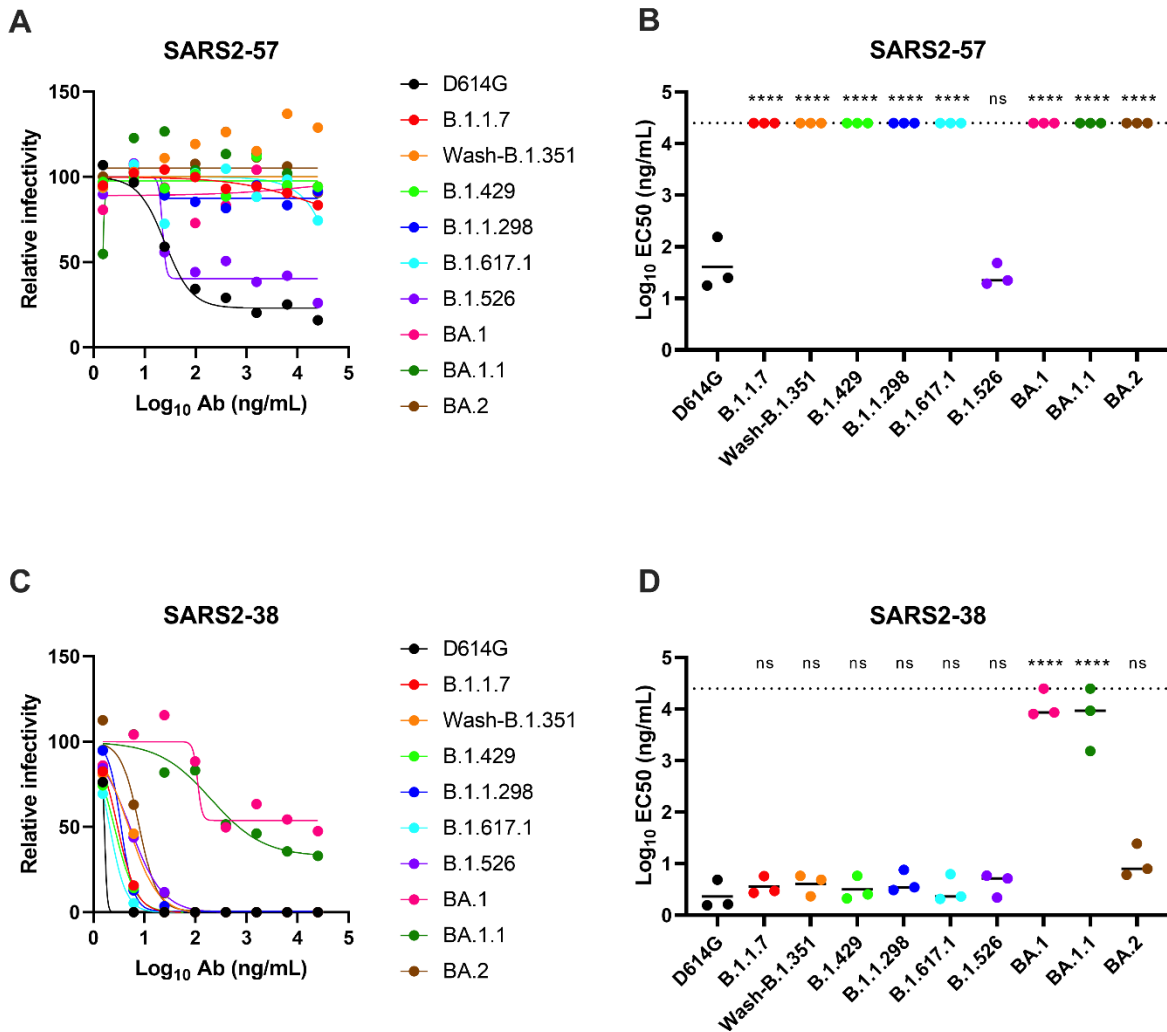
Figure S6. Neutralization of SARS-CoV-2 variants by mAb SARS2-57. Related to Figure 6. SARS2-57 **(A-B)** and SARS2-38 **(C-D)** were tested for neutralization of the indicated variants by FRNT on Vero cells. **(A and C)** Representative dose response curves from one of three experiments are shown. **(B and D)** Mean EC50 values are shown; data are from three independent experiments. Dotted line indicates the limit of detection. EC50 values of dose response curves with resistant fractions >70% were set at the limit of detection. **(B and D)** One-way ANOVA with Dunnett's post-test. *p<0.05; **p<0.01; ****p<0.0001.
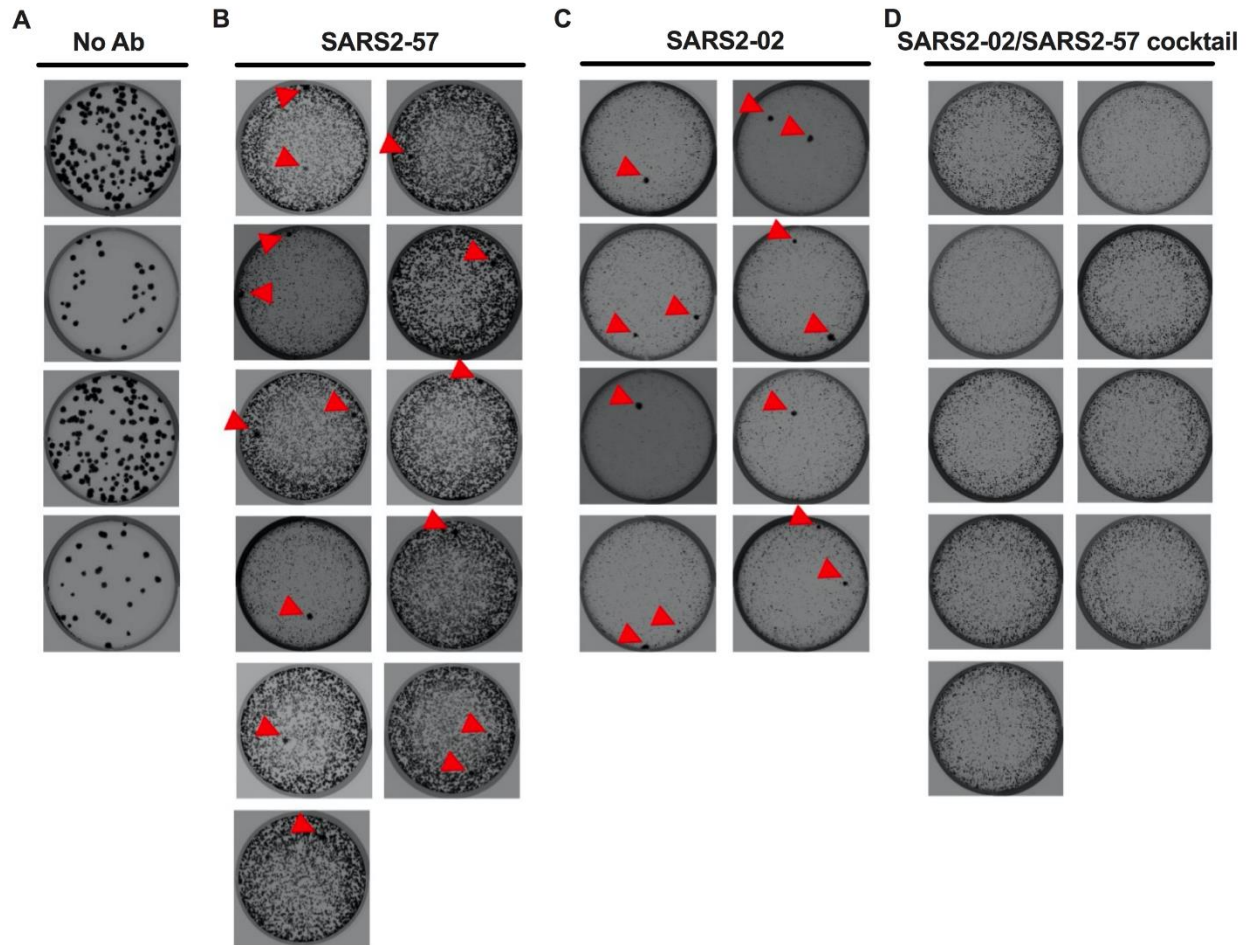
Figure S7. An RBD and NTD mAb cocktail inhibits escape mutant development in vitro. Related to Figure 6. Plaque assays were performed to isolate VSV-SARS-CoV-2-S escape mutants in the presence of **(A)** no antibody, **(B)** NTD mAb SARS2-57, **(C)** RBD mAb SARS2-02, or **(D)** a SARS2-02/SARS2-57 cocktail. Representative images of two experiments are shown. Antibodies were used at a concentration of 62.5 ng/ml for SARS2-2 and 1,389 ng/ml for SARS2-57. Red arrowheads indicated the presence of escape plaques.

Table S1. Cryo-EM data collection, processing, and model refinement statistics. Related to Figure 5.

	SARS-CoV-2 spike + Fv SARS2-57 (full) PDB 7SWX EMD-25488	SARS-CoV-2 NTD + Fv SARS2-57 (local) PDB 7SWW EMD-25487
Data collection		
Magnification	59,000x	59,000x
Exposure (e⁻/Å²)	66.9	66.9
Defocus range (μm)	0.8-2.3	0.8-2.3
Pixel size (Å/pixel)	1.1	1.1
Data processing		
Initial particles (no.)	708,120	708,120
Final particles (no.)	241,481	241,481
Nominal resolution (Å)	3.13	3.13
FSC threshold	0.143	0.143
Model refinement		
Adapted PDB models	7DWY, 7A97	7A97
Model resolution (Å)	1.8 / 3.3	1.7 / 3.6
FSC threshold	0.143 / 0.5	0.143 / 0.5
Model composition		
Non-hydrogen atoms	28,670	4,173
Residues	3,522	511
Ligands (glycans)	81	8
B-factors (Å²)		
Residues	74.11	89.24
Ligands (glycans)	111.12	90.26
Bonds (RMSD)		
length (Å)	0.003	0.003
Angles (°)	0.611	0.735
Validation		
Molprobity score	1.51	1.58
Clash score	6.47	9.42
Rotamer outliers (%)	0.03	0.00
Ramachandran		
Favored (%)	97.16	97.61
Allowed (%)	2.84	2.39
Outliers (%)	0.0	0.00

Respective statistics from MolProbity are provided for focused and global refinements of SARS2-57 Fab bound to SARS-CoV-2 NTD/spike.

Table S2. Close contacts & buried surface area at SARS2-57/NTD interface. Related to Figure 5.

NTD residue	SARS2-57 residue (no. close contacts)	Buried surface area, Å² (% of interface)
Y144	Y102^H(6)	12.4 (1.4%)
Y145	Y102^H(6)	7.3 (0.8%)
H146	Y102^H(1)	41.4 (4.7%)
K147	K30^H(4), D31^H(4), Y32^H(8), F33^H(1), D52^H(1), E54^H(3)	134.1 (15.3%)
N148	D31^H(2), Y32^H(11)	67.1 (7.6%)
M153		3.7 (0.4%)
E156	N33^L(1)	32.7 (3.7%)
R158	Y31^L(1)	25.9 (3.0%)
S247	F33^H(1), E54^H(1), Y102^H(7)	46.5 (5.3%)
Y248	W50^H(6), W99^H(1)	108.3 (12.3%)
L249	Y102^H(4)	84.4 (9.6%)
T250	Y100^L(3)	55.7 (6.3%)
P251	Y31^L(3), Y38^L(2), Y97^L(2), Y98^L(10)	116.7 (13.3%)
G252	Y98^L(3), N99^L(7)	43.9 (5.0%)
D253	Y100^L(3)	37.5 (4.3%)
S256		9.5 (1.1%)
G257		1.8 (0.2%)
NAG[:N149]		49.2 (5.6%)
Total	**102 close contacts**	**878 Å²**

NTD epitope residues were determined via PISA solvent exclusion analysis. Close contact residues of mAb SARS2-57 are listed for each NTD residue, with the number of pairwise atomic contacts noted for each interaction (<3.9 Å cutoff). SARS2-57 residues are superscripted to delineate light chain (L) and heavy chain (H) residues. Buried surface area was calculated using PISA.